博士論文

Electrochemical Properties of MgH_2 and TiH_2 for All-Solid-State Lithium Ion Batteries

（全固体リチウムイオン電池における MgH_2 と TiH_2 の電気化学特性）

川人　浩司

広島大学大学院先端物質科学研究科

2016 年 5 月

目次

主論文

Contents

1 Introduction

1.1 Role of secondary batteries

Following the Great Eastern-Japan Earthquake in 2011, the energy situation of Japan has intensively changed. Due to the halt of nuclear power, energy self-sufficiency ratio in Japan was reduced to 4.4% (Energy self-sufficiency including the nuclear power: 19.5%) in 2011 [1-1]. In order to recover the seriously-deficient energy, Japan needs to import much more fossil fuels, leading to public financial burden. Besides, the fossil fuels have an inevitable essential problem for the greenhouse warming. In this situation, it is important to increase the energy that can be produced in own country, that is to develop renewable energy systems as imperative and urgent issues.

The renewable energy is unstable as an essential problem due to discontinuous energy sources. The energy, for instance, solar power and wind power, depend strongly on the weather, which should become a big problem for a stable power supply. To overcome the problem, it is necessary to develop efficient energy storage devices to balance the supply with the demand. On that point, secondary batteries are useful as energy storage devices. The secondary batteries can store the electrical energy as a chemical energy and easily reconvert it into the electrical energy. In recent years, we have seen quite impressive progress in the development of technology for secondary batteries. However, looking back on the current situation of secondary batteries, the energy density, power density, cost, safety etc., are not enough to meet a recent requirement. Therefore, a lot of researches have been dedicated to investigations and developments for high performance

secondary batteries.

1.2 Lithium ion batteries

Currently, there are various kinds of the secondary batteries, e.g. lead acid, Ni-Cd, nickel-MH (metal hydride), and lithium ion batteries. Figure 1-1 shows the energy density comparison of secondary batteries. Among the secondary batteries, lithium-ion batteries have the highest energy density (more than 100 Wh kg^{-1} and 250 Wh $liter^{-1}$) and excellent cyclability. Therefore, they have been widely used as energy sources for electric devices such as cell phones and laptops. In addition, they have been rapidly spread for large-scale applications such as electric vehicles (EVs) and hybrid electric vehicles (HEVs). Along with the popularization of EVs and HEVs, a market scale of lithium ion batteries is expected to be unprecedentedly expanded. However, in order to match the performances for an internal-combustion engine, the energy density should be improved more than 5 times larger than the present value. Therefore, a lot of research has been conducted to develop new electrode materials for the replacement with the currently used materials.

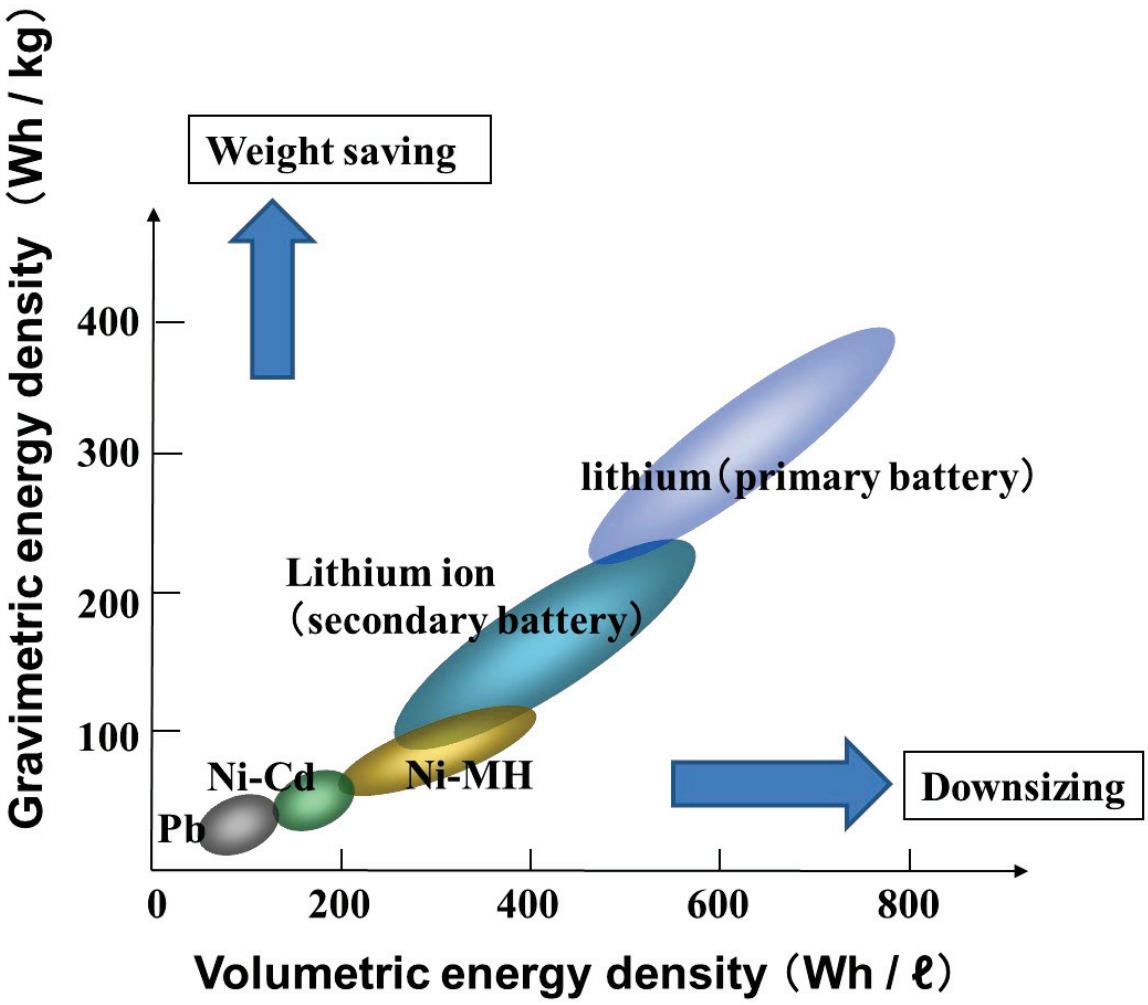

Figure 1-1 Energy density comparison of secondary batteries [1-2]

(Lithium primary battery is shown as reference)

1.2.1 Working principle of lithium ion batteries

Figure 1-2 shows the schematic of operating principle of lithium-ion batteries. Lithium ion batteries generally consist of lithium containing positive electrode (e.g. $LiCoO_2$), negative electrode (e.g. graphite) and electrolyte containing dissociated salts (e.g. $LiPF_6$) as ionic conductor. Positive and negative electrodes are separated by a micro-porous membrane. During the discharge, due to the difference of chemical potentials between the two electrodes, lithium ions move from the negative electrode to the positive electrode through the electrolyte. Simultaneously, to maintain the electroneutrality, electrons move from negative electrode to positive electrode through the external circuit. During the charge process, the reverse process of discharge occurs.

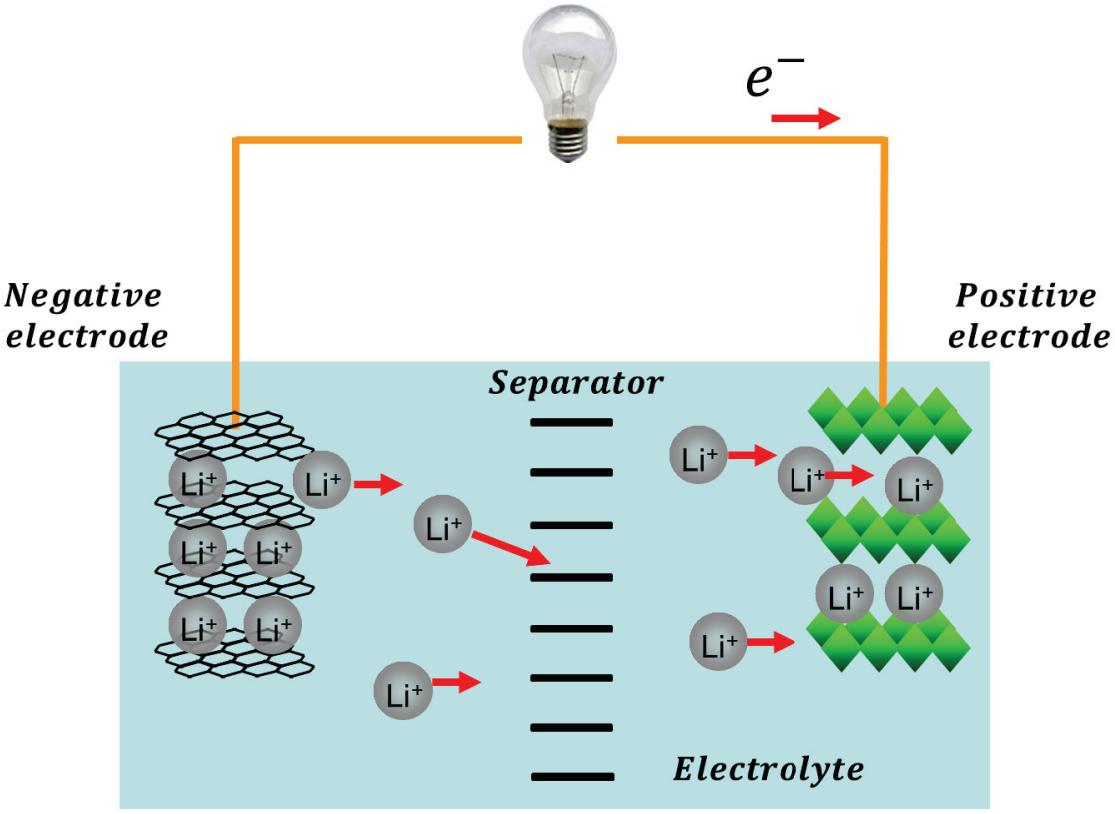

Figure 1-2 Schematic diagram of operating principle for lithium-ion batteries

1.2.2 Thermodynamics

Herein, to understand the thermodynamics of electrochemical reactions during the charge-discharge processes, the electron transfer equilibrium is considered as follows,

$$\mathrm{pP} + \mathrm{qQ} + \ \mathrm{n}e^- \leftrightarrow \ xX + yY, \qquad (1\text{-}1)$$

where P and Q are oxidant, and X and Y are reductant. $\mathrm{P, Q, X, and\ Y}$ exist in solution $(\mathrm{voltage} = E_S)$ and electron exist in electrode $(\mathrm{voltage} = E_M)$. Each electrochemical potential is expressed by the following equations,

$$\mu_P = \mu_P^\circ + RT\ \ln a_P + z_P F E_s, \qquad (1\text{-}2)$$

$$\mu_Q = \mu_Q^\circ + RT\ \ln a_Q + z_Q F E_s, \qquad (1\text{-}3)$$

$$\mu_X = \mu_X^\circ + RT\ \ln a_X + z_X F E_s, \qquad (1\text{-}4)$$

$$\mu_Y = \mu_Y^\circ + RT\ \ln a_Y + z_Y F E_s, \qquad (1\text{-}5)$$

$$\mu_e = \mu_e^\circ + RT\ \ln a_e + z_e F E_M = \mu_e^\circ - F E_M, \qquad (1\text{-}6)$$

$$(\because a_e = 1, z_e = -1\ ),$$

where *a* is activity, *z* is valence and *F* is Faraday constant. Therefore, from the equilibrium reaction (1-1), the equation is expressed as follows,

$$\mathrm{p}\left(\mu_P^\circ + RT\ \ ln a_P + z_P F E_s\right) + \mathrm{q}\left(\mu_Q^\circ + RT\ \ ln a_Q + z_Q F E_s\right) + \mathrm{n}(\mu_e^\circ - F E_M\ \ )$$
$$= \ \mathrm{x}\left(\mu_X^\circ + RT\ \ ln a_X + z_X F E_s\right) + \mathrm{y}\left(\mu_Y^\circ + RT\ \ ln a_Y + z_Y F E_s\right), \tag{1-7}$$

therefore,

$$x\mu_X^\circ + y\mu_Y^\circ - p\mu_P^\circ - q\mu_Q^\circ - n\mu_e^\circ = \mathrm{RT}\ \ln\ \frac{a_P^p}{a_X^x}\frac{a_Q^q}{a_Y^y} + F\left[\left(xz_X + yz_Y - pZ_p - qz_Q\right)E_s + nE_M\right]. \tag{1-8}$$

The left side of the equation can be expressed as ΔG°. Furthermore, considering conservation of charge ($\mathrm{n} = pz_p + qz_Q - \ xz_X - yz_Y$), the equation can be described as follows,

$$\Delta G^\circ = \mathrm{RT}\ \ln\ \frac{a_P^p}{a_X^x}\frac{a_Q^q}{a_Y^y} + nF[E_M - E_s]\ . \tag{1-9}$$

Therefore,

$$E_M - E_S = -\frac{\Delta G^\circ}{nF} - \frac{\mathrm{RT}}{nF}\ \ln\ \frac{a_P^p}{a_X^x}\frac{a_Q^q}{a_Y^y}\ . \tag{1-10}$$

This equation is called “Nernst equation”. Generally, $-\frac{\Delta G^{\circ}}{nF}$ is expressed as standard electrode potential of E°. Since it is impossible to evaluate the absolute value of electrode potential $(E_M - E_S)$, it is expressed by the difference between the electrode potential (E_M) and electrolyte potential (E_S) of lithium in the case of lithium ion batteries. In this way, the electrode potential can be estimated by using thermodynamic parameters of the composed materials.

1.3 All-solid-state lithium batteries

A lot of fire accidents of lithium ion batteries have been reported all over the world. Thermal runaway is one of the reasons for the fire accidents, therefore many studies have been conducted to prevent it [1-3]. Generally, thermal runaway is caused when the exothermic reaction goes out of control between the organic electrolytes and electrodes. In other words, there is a risk of ignition as long as organic electrolytes are used. Then, new ionic conductors such as solid polymer and ionic liquid, which are fire-retardant electrolytes, have been developed. Furthermore, non-flammable solid ceramic electrolytes are considered as ionic conductors for lithium ion batteries. Development of solid electrolytes with high ionic conductivity is one of the important issues to realize all-solid-state lithium ion batteries. Figure 1-3 shows the ionic conductivity of typical ionic conductors. Nowadays, three typical solid electrolytes have been developed, which are oxide, sulfide and hydride-based solid electrolytes.

1.3.1 Solid electrolytes

Oxide-based solid electrolytes are one of the promising lithium ion conductors. Some oxide solid electrolytes such as $La_{0.5}Li_{0.5}TiO_3$ and $LiTi_2(PO_4)_3$ show high ionic conductivity in the order of $10^{-3}\ S\ cm^{-1}$ at room temperature. Moreover, oxides are easy to be handled because they are stable against the moisture. However, most of the oxide-based solid electrolytes have quite low ionic conductivity of $10^{-4} \sim 10^{-6}\ S\ cm^{-1}$ at room temperature and their grain boundary resistance is quite high for battery application.

Sulfide-based solid electrolytes are expected to have better ionic conductivity than oxide-type solid electrolytes because sulfide ions have large polarizability compared with oxide ions, leading to the much weaker interaction between anions and cations (lithium ions). Actually, sulfide-type solid electrolytes show higher ionic conductivities of $10^{-2} \sim 10^{-4}\ S\ cm^{-1}$ than oxide-type solid electrolytes. Another advantage is that the sulfide-based solid electrolytes have quite low grain-boundary resistance due to the softness of the particles. This feature is preferable for making good interface between electrolyte and electrode materials, thus it is expected to be suitable for application to all-solid-state batteries. Recently, Kamaya et al. reported the sulfide-based solid electrolyte of $Li_{10}GeP_2S_{12}$ which has the highest lithium ionic conductivity of $1.2 \times 10^{-2}\ S\ cm^{-1}$ in solid electrolytes [1-4]. This material is called Thio-LISICON (Lithium Super Ionic Conductor). It is considered that sulfide-type solid electrolytes are

feasible from the viewpoint of ionic conductivity. Furthermore, Tatsumisago et al. reported that the Thio-LISICON structure can be produced by using P_2S_5 and Li_2S [1-5]. The developments have been conducted not only to the electrochemical properties but also to synthesis process. The industrialized mass production method for these sulfide-type solid electrolytes has already been considered. Sulfur (S) is a material by-produced in large quantities in the process of petroleum refining. Therefore, if the by-products are used effectively, it can contribute to the improvement of the global environment.

As a hydride-based solid electrolyte, lithium borohydride ($LiBH_4$) has been reported by Matsuo et al.in 2007 [1-6]. Although $LiBH_4$ is an electric and ionic insulator at low temperature, only the ionic conductivity drastically increases three orders of magnitude over 115 °C as shown Figure 1-4. It is considered that structural change is concerned to the ionic conductivity. $LiBH_4$ has the phase transition from the low temperature phase of orthorhombic to the high temperature phase of hexagonal at 115 °C. As shown in Figure 1-5 [1-6], the nearest neighbor of Li arranges along the *a* and *b* axes without hindrance in the high temperature phase. The rearrangement might enable the Li^+ to migrate along each axis. To realize the high ionic conduction state at room temperature, it has been done that $[BH_4]^-$ complex ions of $LiBH_4$ is partially replaced with I^- ions to stabilize the hexagonal phase. Figure 1-6 shows the ionic conductivities of $Li(BH_4)_{0.75}I_{0.25}$ and other complex hydrides [1-7]. Besides $LiBH_4$, a large number of hydride-based solid electrolytes have been reported. Due to the many variations of anion species, there are a lot of possibilities of design for high lithium ionic conductor.

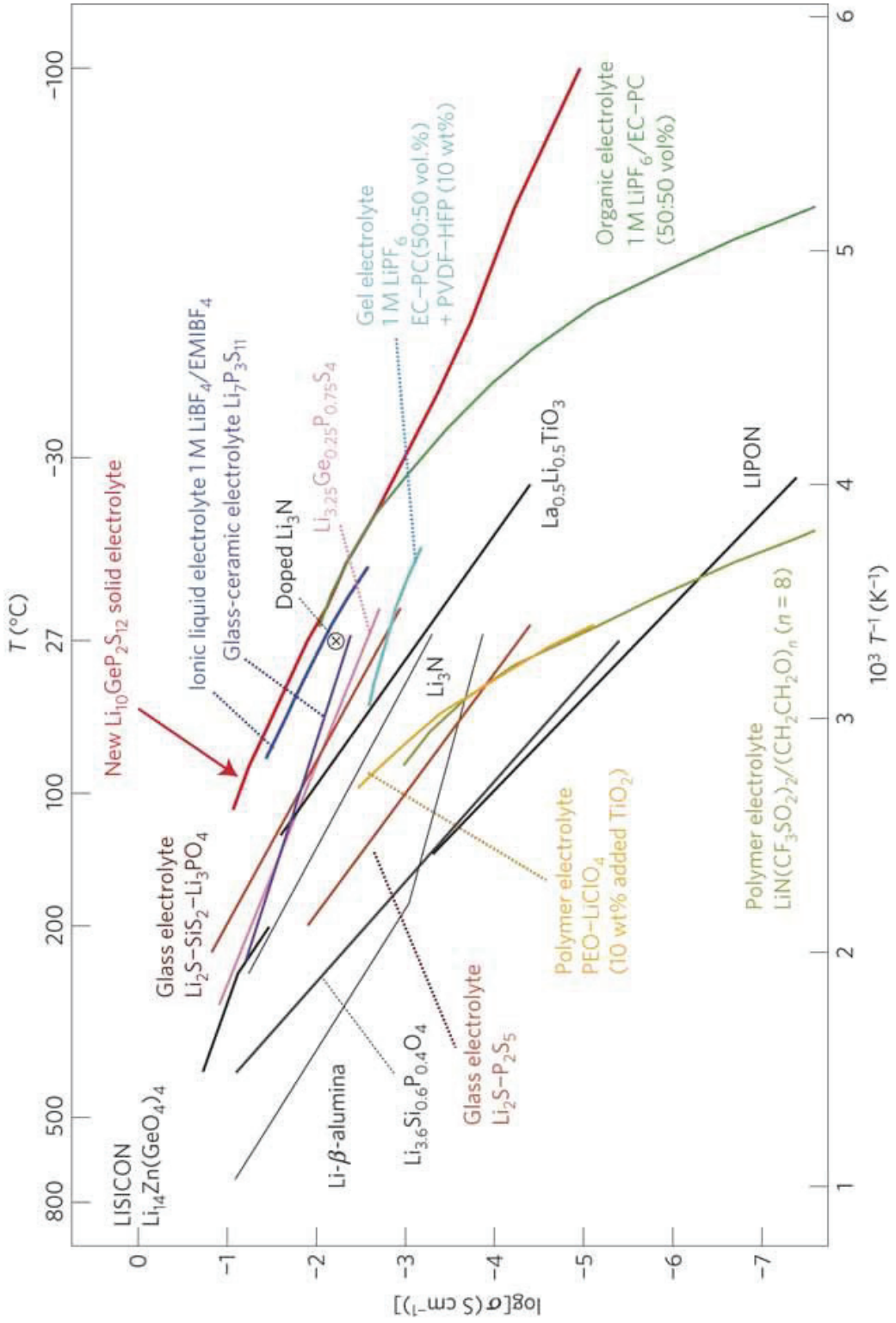

Figure 1-3 Ionic conductivity of various lithium ion conductors [1-4]

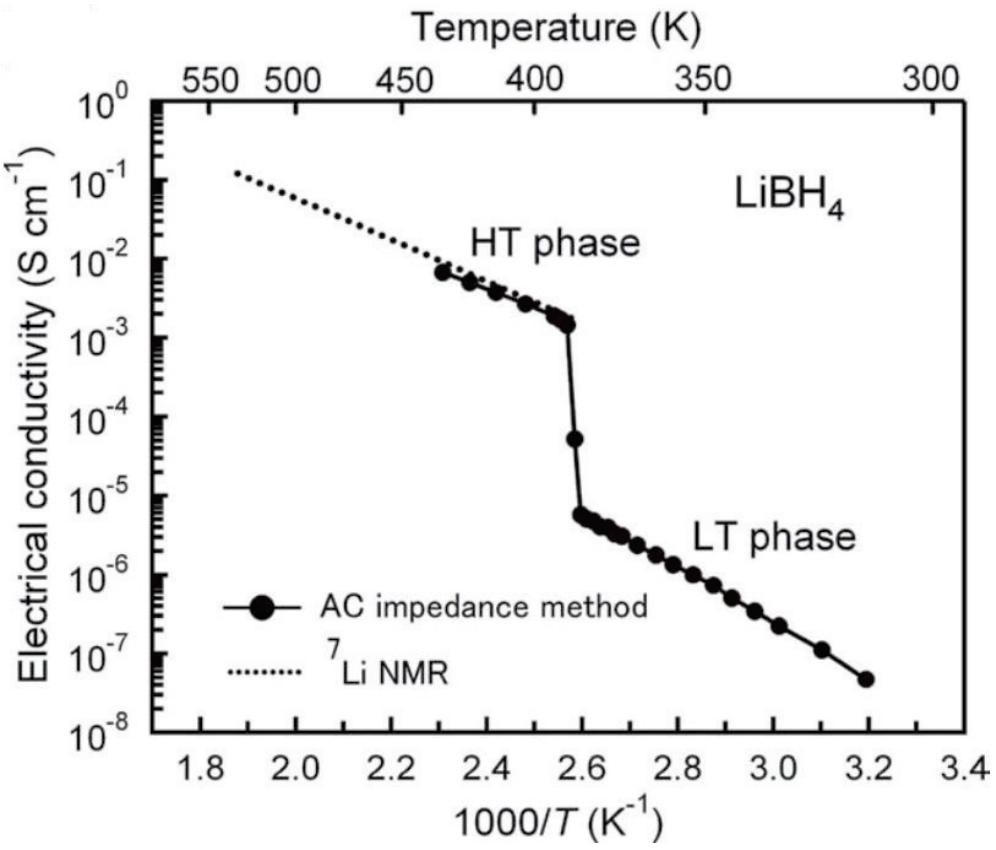

Figure 1-4 Ionic conductivity of $LiBH_4$ [1-6]

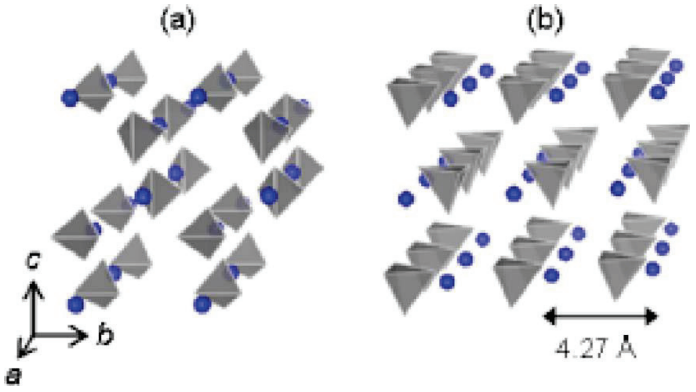

Figure 1-5 Crystal structures of $LiBH_4$ in (a) orthorhombic (low temperature phase) and (b) hexagonal (high temperature phase). Blue ball and gray tetrahedron show Li and BH_4, respectively [1-6]

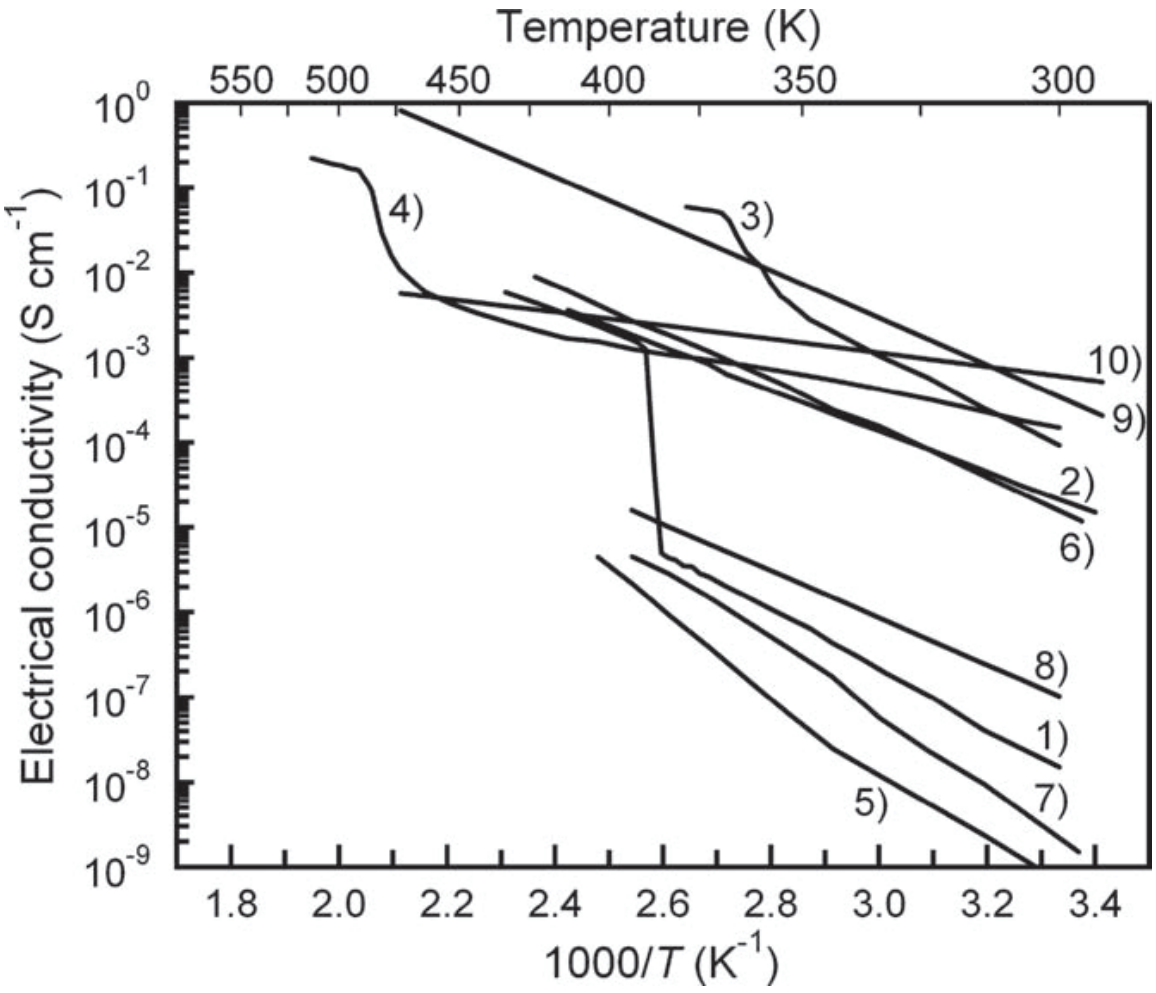

Figure 1-6 Lithium ionic conductivities of complex hydrides: 1) $LiBH_4$, 2) $Li(BH_4)_{0.75}I_{0.25}$ ($LiBH_4$–LiI system), 3),4) $Li_2(BH_4)(NH_2)$ and $Li_4(BH_4)(NH_2)_3$ ($LiBH_4$ – $LiNH_2$ system), 5),6) $LiNH_2$ and $Li_3(NH_2)_2I$ ($LiNH_2$-based complex hydrides), and 7),8) $LiAlH_4$ and Li_3AlH_6 ($LiAlH_4$ -based complex hydrides). For reference, the data of related compounds are also shown: 9) Li_2NH and 10) Li_3N [1-7]

1.4 Negative electrodes for lithium ion batteries

Lithium metal has the largest capacity as the negative electrode. Furthermore, lithium has the largest ionization tendency, in other words, it shows the lowest electrode voltage against the positive electrode. Thus, lithium metal is expected to be the best negative electrode for lithium ion batteries. However, if lithium metal is used as the negative electrode, it grows as dendrite in the deposition process of lithium (charge process). As a result, the dendrite penetrates a separator and induces an internal short circuit between the positive and negative electrode. Indeed, the cell phone using lithium metal negative electrode had fire accident caused by internal short circuit in 1989. To prevent such accident, carbon-based negative electrodes were developed which store the lithium ion with insertion / de-insertion reaction. Today, various kinds of negative electrodes such as alloying / de-alloying and conversion type negative electrodes have been developed to improve not only the safety of lithium ion batteries but also their energy density.

1.4.1 Intercalation / de-intercalation type negative electrodes

Due to the simple and high reversible electrochemical reactions, intercalation / de-intercalation type negative electrodes are widely used as negative electrodes for commercial lithium ion batteries. Although they have intrinsic problem of low theoretical lithium accommodate capacity due to its limitation of structural change by the reaction with the lithium, there are no alternatives to their quite high reversibility.

•Graphite

Numerous researches have been conducted extensively for the clarification of the reaction mechanism between lithium and graphite [1-8-11]. Graphite is composed of multi layered structure of graphene, which can reversibly store the lithium between its layers as intercalation. Figure 1-7 shows schematic diagram illustrating the staging phenomenon [1-12]. Depending on the lithium storage ratio, graphite has four kinds of stage, finally leading to a theoretical capacity of 372 mAh g^{-1}. One lithium is intercalated per six carbons, which is the maximum concentration of lithium for the graphite negative electrode. The equilibrium potential of the reaction is around 0.1 V vs. Li^+/Li. Graphite shows not only suitable equilibrium potential for negative electrode but also good coulombic efficiency, high reversible capacity, and long cycling life. Furthermore, it can be provided at a low cost since carbon is abundant material in the universe. Due to the excellent features, graphite is commercially used as negative electrode for recent lithium ion batteries.

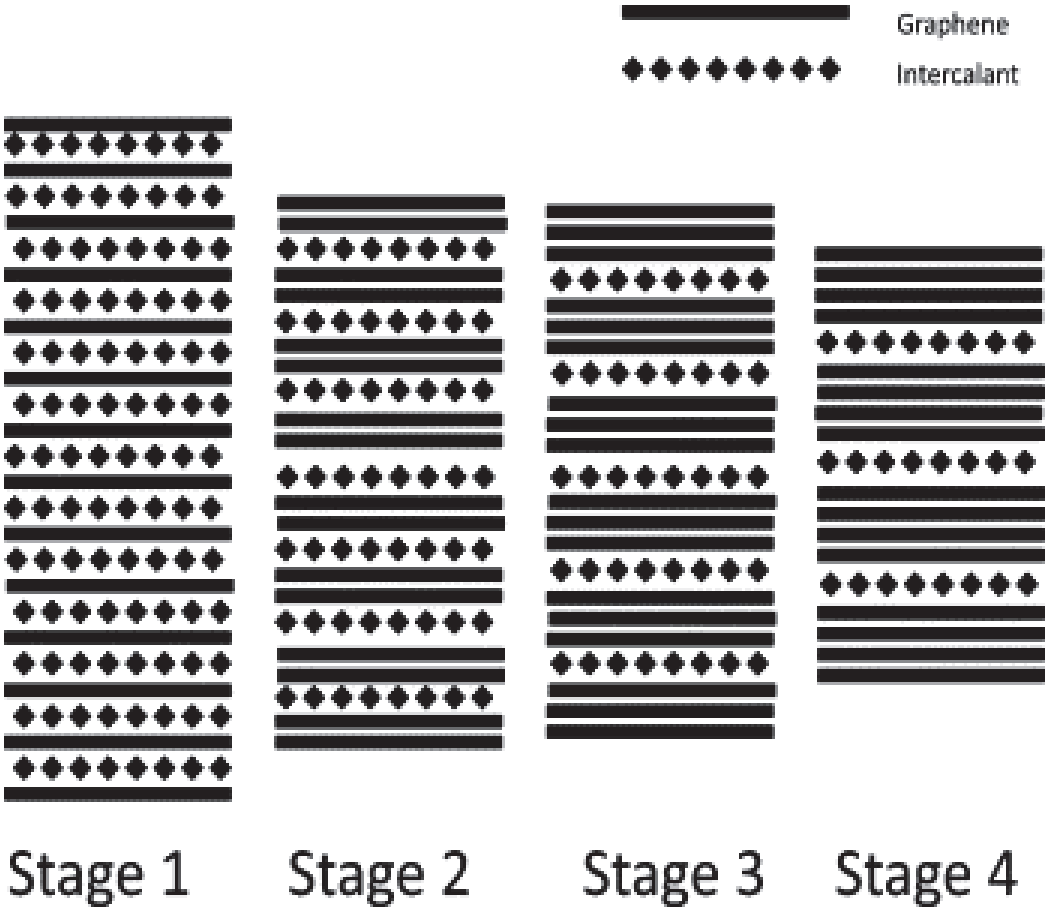

Figure 1-7 Schematic diagram illustrating the staging phenomenon of graphite [1-12]

1.4.2 Alloying / de-alloying type negative electrodes

Various kinds of electrochemical reactions between lithium and metals, (Mg, Ca Al, Si, Ge, Sn, Pb, As, Sb, Bi, Ag, Au, Zn, Cd, Hg, etc.) have been investigated so far [1-13]. All the lithium-metal alloys have quite high specific capacity compared with graphite negative electrode. However, the disadvantage is that they have large volume expansion by the reaction with lithium. The physical stress induces the poor contact among active material, electro-conductive material, and current collector, resulting that the electrodes have poor reversible capacity and cycling life. To overcome the problem, a lot of attempts have been done related to morphology modification.

•Silicon

Silicon is considered as a promising negative electrode since it has quite high theoretical gravimetric capacity (4200 mAh g^{-1}) and volumetric capacity (9786 mAh cm^{-1}) among the negative electrode materials. Furthermore, it has a low equilibrium potential around 0.3 ~ 0.05 V vs. Li^+/Li. Figure 1-8 shows the theoretical charge-discharge profile of silicon negative electrode [1-14]. It was reported that the large theoretical capacity due to the formation of intermetallic state such as $Li_{12}Si_7$, Li_7Si_3, $Li_{13}Si_4$, $Li_{22}Si_5$. However, it is reported that the capacity decreases down to 200 mAh g^{-1} after only 10 cycles [1-15]. As mentioned above, it has a quite large volume change during litiation (＜400%), leading to rapid drop of the capacity. To overcome this problem, extensive researches for morphology modification have been performed, for example, Si

nanowires and nanotubes showed quite high reversible capacity around 2000 mAh g^{-1} over 50 cycles [1-16]. The continual development of the strategy is important issue to realize a practical utilization of silicon as negative electrode for lithium ion batteries.

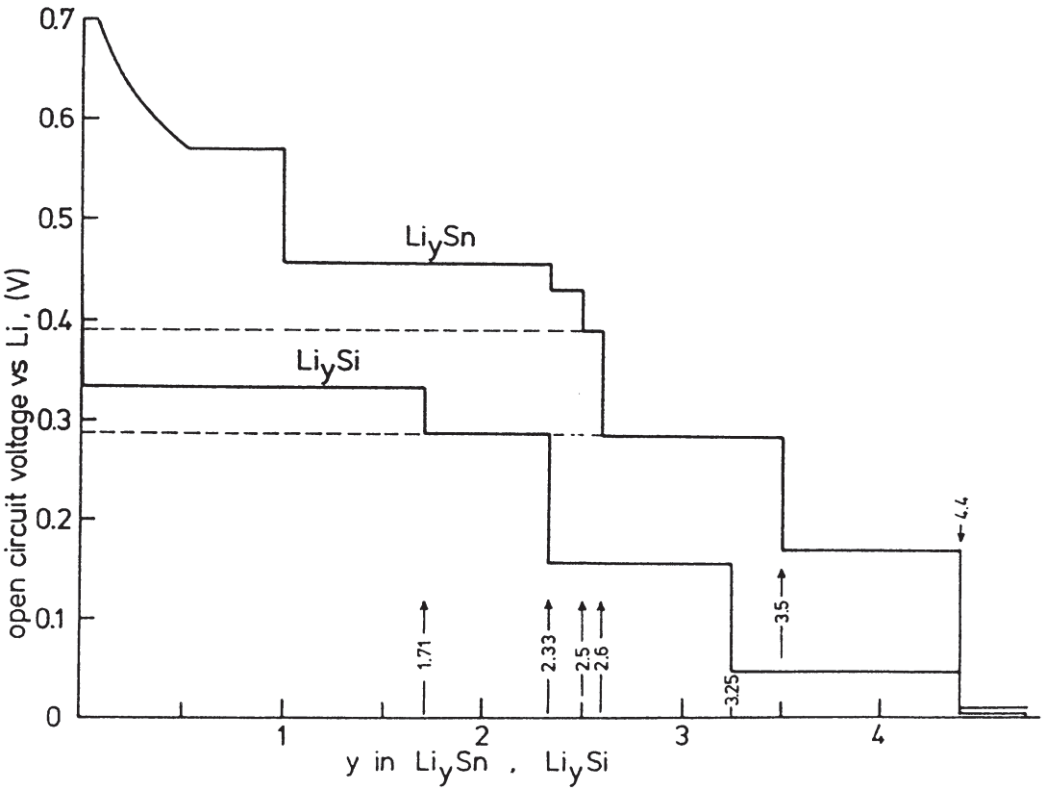

Figure 1-8 Theoretical charge-discharge profiles of silicon and tin negative electrode

[1-14]

1.4.3 Conversion type negative electrodes

Conversion-type negative electrodes have been studied as is indicated by the following reaction [1-17, 18],

$$M_xX_y + \ n\ Li^+ + n\ e^- \rightarrow xM + Li_nX_y, \qquad (1\text{-}11)$$

$$M = \text{Metal}\ \ (\text{Mg, Cr, Mn, Fe, Ni, Co, etc.}),$$

$$X = \text{Anion}\ \ (\text{O, S, N, P, F, H}).$$

The reaction has more than one electron per redox-center which leads to much higher lithium storage capacity compared with graphite negative electrodes. While such conversion-type electrode materials are expected to have a large electrode capacity, low energy efficiency in the charge-discharge processes is thought as a considerable problem, which could come from large polarization during the processes. In a previous work, it is reported that the charge-discharge hysteresis decreases by the anion moving from fluorides ($\Delta V \approx 1.5$ V) to oxides ($\Delta V \approx 0.8$ V), sulfides ($\Delta V \approx 0.6$ V), phosphides ($\Delta V \approx 0.4$ V), and hydrides ($\Delta V \approx 0.2$ V), meaning that the hysteresis has a tendency associated with electro-negativity and polarizability of X^{m-} species [1-17, 19] as shown Figure 1-9. Conversion type negative electrodes could be regarded as new candidates for negative electrode of lithium ion batteries since large numbers of combination can be considered for this system.

•Cobalt Oxide

Cobalt oxide (Co_3O_4) is the most studied negative electrode among the conversion type negative electrodes. It has a theoretical capacity of 890 mAh g^{-1} with equilibrium potential around 1 V vs. Li^+/Li. However, due to the large charge-discharge hysteresis ($\Delta V \approx 0.8$ V) , high degradation of cycleability of the conversion reaction was reported. Various kinds of attempts for solving the problem have been done by controlling morphology (porous nanostructure [1-20, 21], nanowires [1-22]) and coating with carbon materials [1-23]. As results, smaller particle size and coating with conductive materials improve the electrochemical properties of Co_3O_4. Although a lot of improvements have been conducted on the conversion reaction, the properties of oxides showing low electro-conductivity remain an inherent issue.

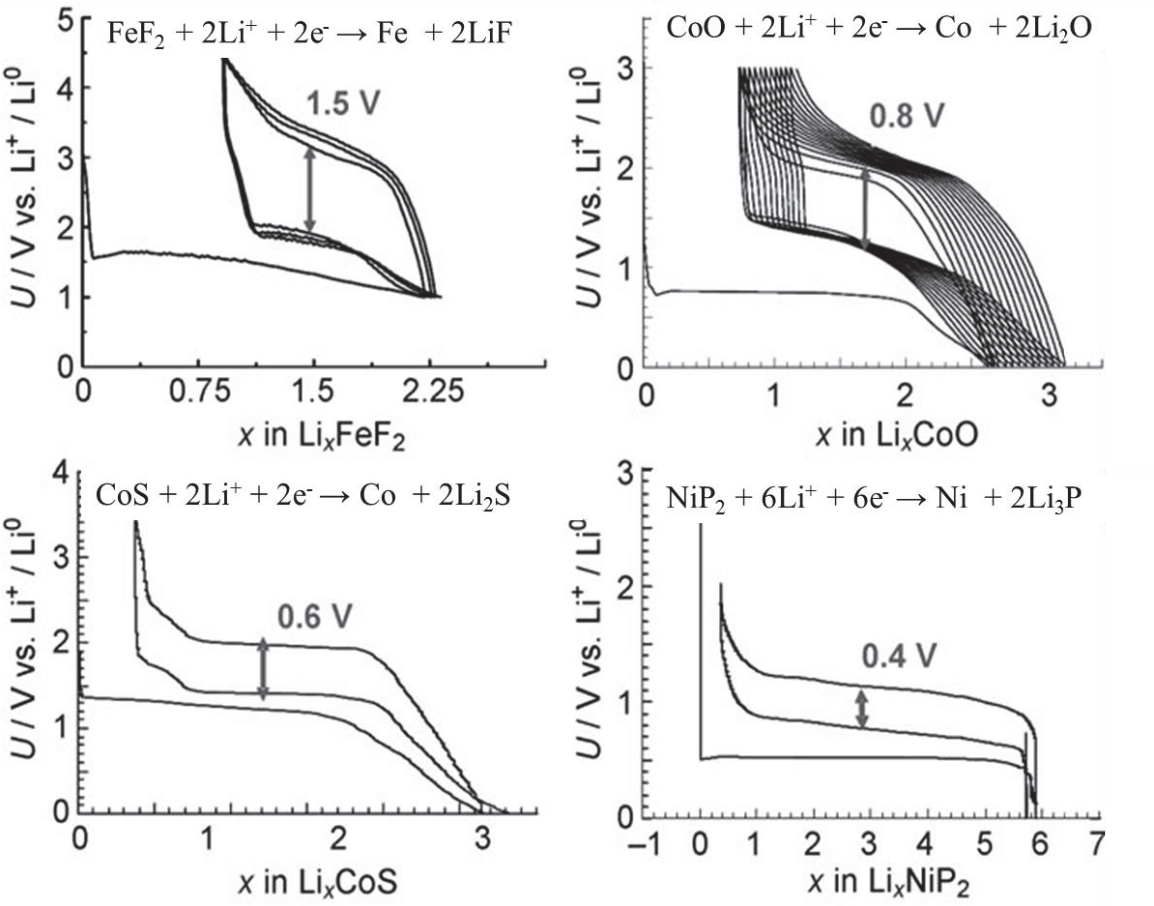

Figure 1-9 Voltage composition profiles for a representative binary fluoride, oxide, sulfide, and phosphide [1-19]

1.5 Metal hydrides

Metal hydrides have been researched in hydrogen storage field for a long time since it can reversibly absorb and desorb hydrogen. Whereas, quite recently, new characteristic of metal hydrides was reported, that is, the hydrides reversibly react with lithium and act as electrode for lithium ion batteries [1-24]. Metal hydrides are categorized as conversion type negative electrodes since it has a following reaction,

$$\mathrm{MHx} + \mathrm{x}Li^{+} + xe^{-} \rightarrow \mathrm{M} + \mathrm{xLiH}, \qquad (1\text{-}12)$$

$$\mathrm{M} = \mathrm{Metal}\ (\mathrm{Mg, Ti, Na, Zr, etc.}).$$

By using the Nernst law: $\mathrm{E} = -\Delta_{\mathrm{r}}G^{\circ}/xF$, the equilibrium potential is calculated as follows,

$$\mathrm{MHx} + \mathrm{xLi} \rightarrow \mathrm{M} + \mathrm{xLiH}: \ \Delta_{\mathrm{r}}G^{\circ}. \qquad (1\text{-}13)$$

The Gibbs free energy of the reaction in equation (1-13) is,

$$\Delta_{\mathrm{r}}G^{\circ} = [\ \Delta_{\mathrm{f}}G^{\circ}(\mathrm{M}) + \ \mathrm{x}\Delta_{\mathrm{f}}G^{\circ}(\mathrm{LiH})] - \ [\Delta_{\mathrm{f}}G^{\circ}(\mathrm{MHx}) \ + \mathrm{x}\Delta_{\mathrm{f}}G^{\circ}(\mathrm{Li})]$$

$$= \ \mathrm{x}\Delta_{\mathrm{f}}G^{\circ}(\mathrm{LiH}) - \Delta_{\mathrm{f}}G^{\circ}(\mathrm{MHx}) \ . \qquad (1\text{-}14)$$

Therefore, the reaction is feasible in the case of $\Delta_{\mathrm{f}}G^{\circ}(\mathrm{MHx}) > x\Delta_{\mathrm{f}}G^{\circ}(\mathrm{LiH}: -68.4\ kJ\ mol^{-1})$ as shown in Figure 1-10 [1-25].

Among the metal hydrides, especially, magnesium hydride (MgH_2) has a high theoretical capacity of 2038 mAh g^{-1} with relatively low volume expansions (<200%). Indeed, Y. Oumellal et al. investigated the charge-discharge performance of MgH_2 as negative electrode for lithium ion batteries and it showed large reversible capacity of 1480 mAh g^{-1} at an average voltage of 0.5 V vs. Li^+/Li by following reaction, ($MgH_2 + 2Li^+ + 2e^- \leftrightarrow Mg + 2LiH$) [1-24]. However, the capacity rapidly fades and reduces to less than 200 mAh g^{-1} after only 10 full cycles. In order to overcome these disadvantages, it was reported by this group that stiff polymer binder of carboxymethylcellulose (CMC) was used [1-26] and MgH_2 particle size was controlled [1-27] to obtain higher cyclability. Although they showed better electrochemical properties than those reported in the original paper [1-24], the expected ability for this system was not obtained yet.

Another strong candidate of metal hydrides for negative electrode is titanium hydride (TiH_2), which has a theoretical capacity of 1074 mAh g^{-1} with theoretical potential of 0.163 V versus Li^+/Li by the following reaction, ($TiH_2 + 2Li^+ + 2e^- \leftrightarrow Ti + 2LiH$) [1-28]. In the view point of high power battery, it is preferable as negative electrode since the theoretical potential is quite low compared with MgH_2. However, the cycle properties have not been reported yet due to the low reversibility. Generally, reduction of particle size and addition of electro-conductive materials improve the charge-discharge performance. Meanwhile, these strategies were not effective for the reversibility of the TiH_2 conversion reaction [1-29, 30].

Although metal hydrides have not showed sufficient electrochemical properties yet,

they have the advantage of high capacity and low equilibrium potential. Furthermore, these hydrides have the lowest polarization between charge and discharge ($\Delta V \approx 0.2$ V) compared with other conversion type negative electrodes, therefore, they are promising candidate as negative electrodes for lithium ion batteries.

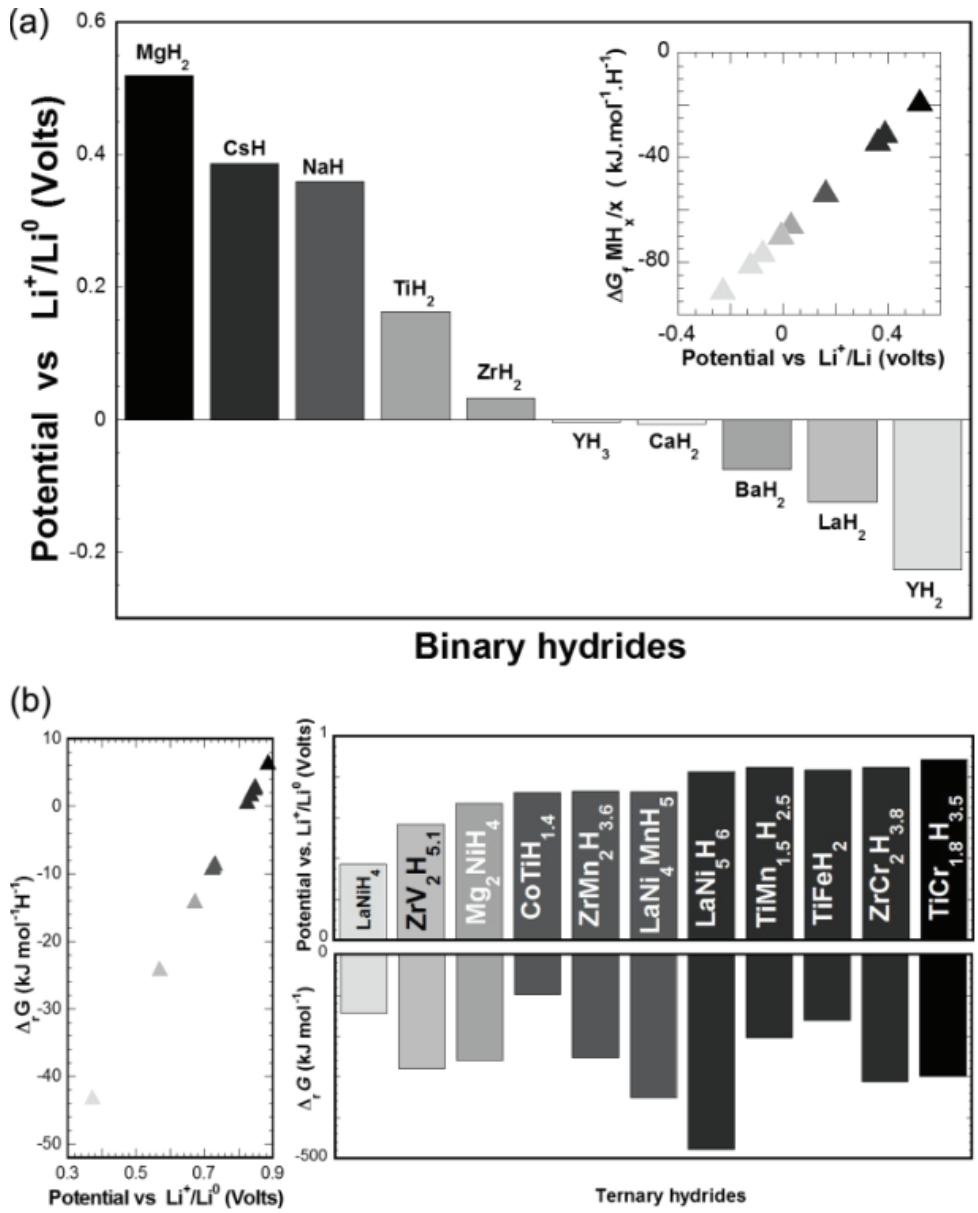

Figure 1-10 Theoretical equilibrium potential for the MH_x/Li cell vs Li^+/Li. a) For binary hydrides M = Y, La, Ba, Ca, Zr, Ti, Na, Cs, Mg. Inset: Gibbs free formation enthalpy of these hydrides as a function of the equilibrium potential. b) For ternary hydrides Mg_2NiH_4, $LaNiH_4$, $CoTiH_{1.4}$, $TiFeH_2$, $ZrV_2H_{5.1}$, $ZrCr_2H_{3.8}$, $ZrMn_2H_{3.6}$, $TiMn_{1.5}H_{2.5}$, $TiCr_{1.8}H_{3.5}$, $LaNi_5H_6$, $LaNi_4MnH_5$ [1-25]

1.6 Hydrogen exchange effect

As mentioned above, metal hydrides have been focused as negative electrodes for lithium ion batteries. When searching for a suitable medium to achieve such a reversible hydride conversion reaction, Li^+ conductivity is an important factor to be considered, and another important factor should be H^- conductivity. As we know, the MgH_2–$LiBH_4$ composite is a well-known material in the hydrogen storage field. In this system, the mobility of H^- in MgH_2 can be strongly enhanced by $LiBH_4$, leading to a superior hydrogen exchange effect between MgH_2 and $LiBH_4$ [1-31]. Figure 1-11 shows the results of in-situ IR spectroscopy for MgD_2-$LiBH_4$ composite. With the increasing temperature, the peak corresponding to the B-D stretching vibration (~1688 cm^{-1}) was found at 275 °C. This result indicated H atoms of $[BH_4]^-$ anions were exchanged for D atoms in MgD_2 even below melting point of $LiBH_4$ (~280 °C). It is considered that this effect may lead to excellent H^- conductivity when applying this material as a negative electrode for lithium ion batteries.

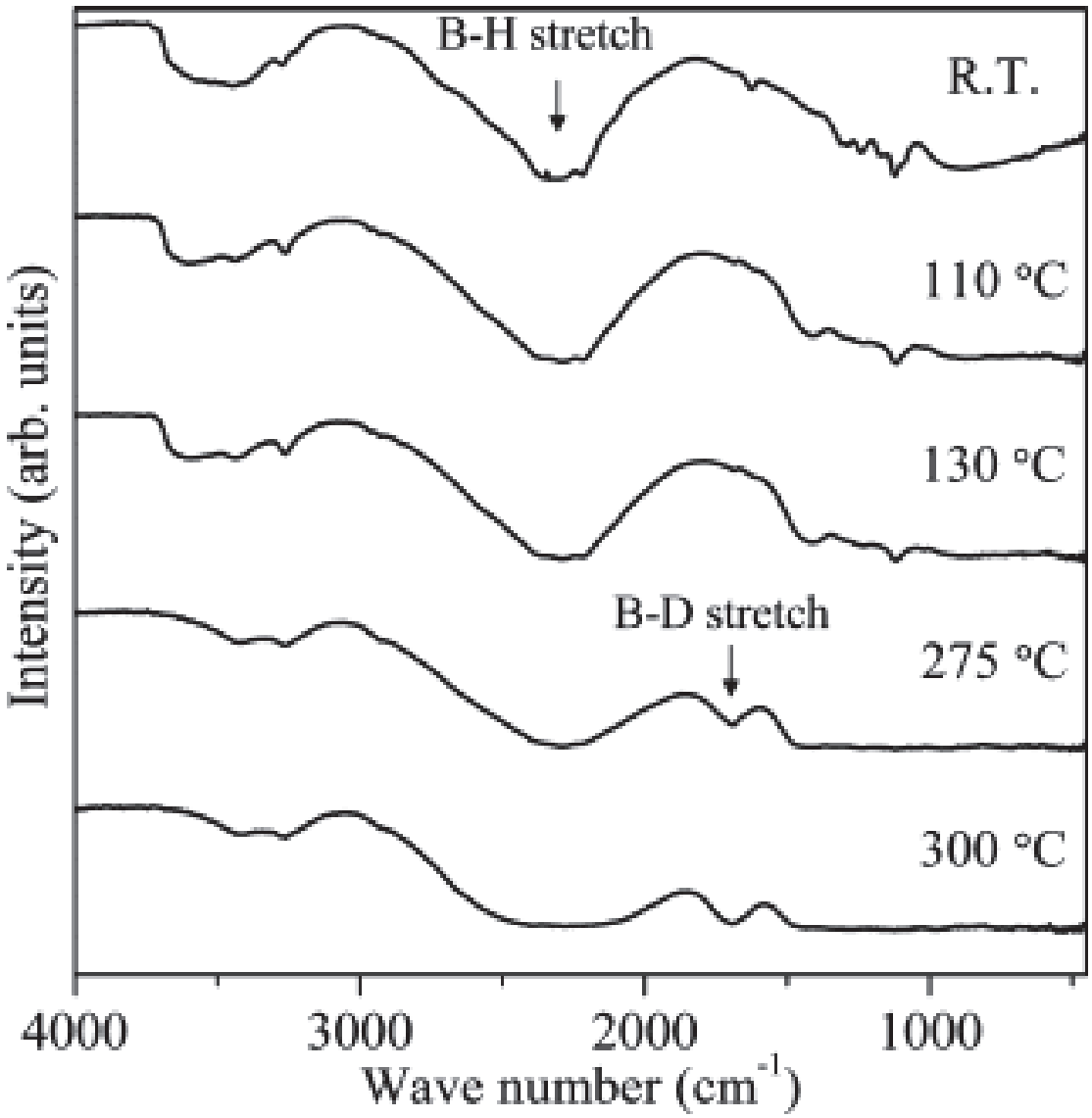

Figure 1-11 In-situ FT-IR spectra of the MgD_2-$2LiBH_4$ composite [1-31]

[1-1] http://www.nedo.go.jp/content/100544816.pdf.

[1-2] J.M. Tarascon, M. Armand, Nature, 414 (2001) 359-367.

[1-3] Q.S. Wang, P. Ping, X.J. Zhao, G.Q. Chu, J.H. Sun, C.H. Chen, J. Power Sources, 208 (2012) 210-224.

[1-4] N. Kamaya, K. Homma, Y. Yamakawa, M. Hirayama, R. Kanno, M. Yonemura, T. Kamiyama, Y. Kato, S. Hama, K. Kawamoto, A. Mitsui, Nat Mater, 10 (2011) 682-686.

[1-5] K. Minami, F. Mizuno, A. Hayashi, M. Tatsumisago, Solid State Ionics, 178 (2007) 837-841.

[1-6] M. Matsuo, Y. Nakamori, S. Orimo, H. Maekawa, H. Takamura, Appl. Phys. Lett., 91 (2007) 224103.

[1-7] M. Matsuo, S. Orimo, Advanced Energy Materials, 1 (2011) 161-172.

[1-8] J.R. Dahn, T. Zheng, Y.H. Liu, J.S. Xue, Science, 270 (1995) 590-593.

[1-9] T. Ohzuku, Y. Iwakoshi, K. Sawai, J. Electrochem. Soc., 140 (1993) 2490-2498.

[1-10] D. Aurbach, B. Markovsky, I. Weissman, E. Levi, Y. Ein-Eli, Electrochimica Acta, 45 (1999) 67-86.

[1-11] H. Nakagawa, Y. Domi, T. Doi, M. Ochida, S. Tsubouchi, T. Yamanaka, T. Abe, Z. Ogumi, J. Power Sources, 236 (2013) 138-144.

[1-12] R. Sengupta, M. Bhattacharya, S. Bandyopadhyay, A.K. Bhowmick, Prog. Polym. Sci., 36 (2011) 638-670.

[1-13] C.M. Park, J.H. Kim, H. Kim, H.J. Sohn, Chem. Soc. Rev., 39 (2010) 3115-3141.

[1-14] R.A. Huggins, J. Power Sources, 81 (1999) 13-19.

[1-15] U. Kasavajjula, C. Wang, A.J. Appleby, J. Power Sources, 163 (2007) 1003-1039.

[1-16] J.R. Szczech, S. Jin, Energy Environ. Sci., 4 (2011) 56-72.

[1-17] R. Malini, U. Uma, T. Sheela, M. Ganesan, N.G. Renganathan, Ionics, 15 (2009) 301-307.

[1-18] J. Cabana, L. Monconduit, D. Larcher, M.R. Palacin, Adv. Mater., 22 (2010) E170-192.

[1-19] P.G. Bruce, B. Scrosati, J.M. Tarascon, Angew. Chem. Int. Ed. Engl., 47 (2008) 2930-2946.

[1-20] W. Yuan, D. Xie, Z. Dong, Q. Su, J. Zhang, G. Du, B. Xu, Mater. Lett., 97 (2013) 129-132.

[1-21] F. Wang, C. Lu, Y. Qin, C. Liang, M. Zhao, S. Yang, Z. Sun, X. Song, J. Power Sources, 235 (2013) 67-73.

[1-22] C.C. Li, Q.H. Li, L.B. Chen, T.H. Wang, J. Mater. Chem., 21 (2011) 11867-11872.

[1-23] X. Liu, S.W. Or, C. Jin, Y. Lv, W. Li, C. Feng, F. Xiao, Y. Sun, Electrochimica Acta, 100 (2013) 140-146.

[1-24] Y. Oumellal, A. Rougier, G.A. Nazri, J.M. Tarascon, L. Aymard, Nat. Mater., 7 (2008) 916-921.

[1-25] L. Aymard, Y. Oumellal, J.P. Bonnet, Beilstein J. Nanotechnol., 6 (2015) 1821-1839.

[1-26] W. Zaïdi, Y. Oumellal, J.P. Bonnet, J. Zhang, F. Cuevas, M. Latroche, J.L. Bobet,

L. Aymard, J. Power Sources, 196 (2011) 2854-2857.

[1-27] Y. Oumellal, C. Zlotea, S. Bastide, C. Cachet-Vivier, E. Leonel, S. Sengmany, E. Leroy, L. Aymard, J.P. Bonnet, M. Latroche, Nanoscale, 6 (2014) 14459-14466.

[1-28] Y. Oumellal, A. Rougier, J.M. Tarascon, L. Aymard, J. Power Sources, 192 (2009) 698-702.

[1-29] Y. Oumellal, W. Zaidi, J.P. Bonnet, F. Cuevas, M. Latroche, J. Zhang, J.L. Bobet, A. Rougier, L. Aymard, Int. J. Hydrogen Energy, 37 (2012) 7831-7835.

[1-30] F.M. Vitucci, A. Paolone, S. Brutti, D. Munao, L. Silvestri, S. Panero, P. Reale, J. Alloys Compd., 645 (2015) S46-S50.

[1-31] L. Zeng, H. Miyaoka, T. Ichikawa, Y. Kojima, J. Phys. Chem. C, 114 (2010) 13132-13135.

2 Purpose

Metal hydrides have been studied as conversion-type negative electrode materials for lithium ion batteries owing to their high theoretical Li storage capacities (>1000 mA h g^{-1}), relatively low volume expansions (<200%) and suitable working potentials (0.1–1.0 V vs. Li^+/Li). In particular, MgH_2 and TiH_2 have been paid much attention as the negative electrode. However, the improvement of the cyclability is one of the important issues to realize its practical application. In this thesis, electrochemical properties of MgH_2 and TiH_2 are investigated by using $LiBH_4$ solid electrolyte. As mentioned in the introduction chapter, the mobility of H^- in MgH_2 in the MgH_2–$LiBH_4$ composite system, can be strongly enhanced by $LiBH_4$, leading to a superior hydrogen exchange effect between MgH_2 and $LiBH_4$. It is considered that this effect may lead to excellent H^- conductivity when applying this material as a negative electrode for lithium ion batteries. Meanwhile, it was reported that $LiBH_4$ exhibited a remarkably high Li^+ conductivity on the order of 10^{-3} S cm^{-1} in its high temperature phase which can be considered as a promising solid-state electrolyte for lithium ion batteries. The combination of the above two effects attracts attention as a system to possibly improve the electrochemical properties.

3 Experimental procedures

3.1 Sample preparation

3.1.1 Materials

Starting materials used in this work are listed in Table 3-1. All the samples were handled in an Ar-filled glove box (>99.9999%) to avoid oxidation and water adsorption.

Table 3-1 General information of materials

Material	Purity, State	Company
Magnesium hydride (MgH_2)	98%, powder	Alfa Aesar
Titanium hydride (TiH_2)	98%, powder	Sigma-Aldrich
Lithium borohydride ($LiBH_4$)	95%, powder	Sigma-Aldrich
Niobium oxide (Nb_2O_5)	99.5%, powder	Sigma-Aldrich
Lithium foil (Li)	99.8%, disc (φ:15 mm)	Honjo Metal
Acetylene black	powder	
Potassium bromide (KBr)	99%, powder	Sigma-Aldrich
Heavy hydrogen (D_2)	99.6%, gas	

3.1.2 Preparation of composite electrodes

Composite electrodes were prepared by mechanical ball-milling method as follows. Firstly, MgH_2 or TiH_2 was weighed to be 300 mg, and placed into Cr-steel ball-milling pot (volume of 30 mL) with 20 zirconia balls (diameter of 8 mm). After that, the samples were mechanically milled for 20 h with 370 rpm by a planetary ball-milling apparatus as shown Figure 3-1. As the reason for this treatment, it was reported that an amorphous nature of the active materials for an electrode lead to improved electrochemical ability

for a conversion reaction of hydride [3-1]. In addition, in the case of MgH_2, it was catalyzed by Nb_2O_5 in order to increase the reactivity of hydriding and dehydriding [3-2]. Then, these active materials were placed into ball-milling pot together with $LiBH_4$ as solid electrolyte and acetylene black as electro-conducting material in a weight ratio of 40:30:30, respectively, to have a total amount of 200 mg. The mechanical milling was conducted for 2 hours to make homogeneous composite electrodes.

.

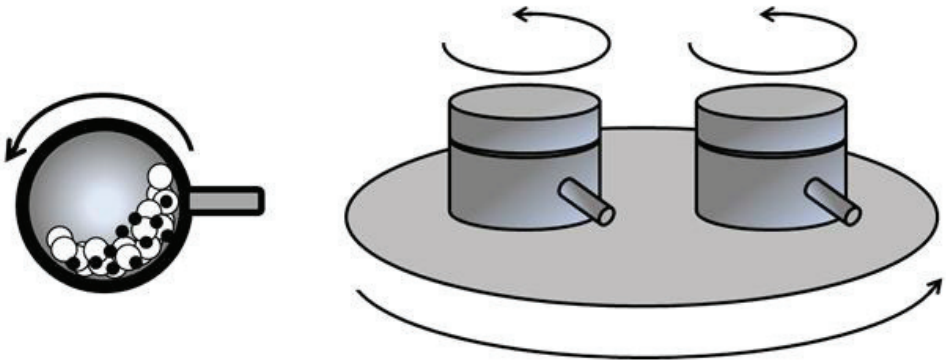

Figure 3-1 Schematic view of the planetary ball-milling apparatus

3.1.3 Preparation of TiD_2-$LiBH_4$ composite

TiH_2 was heated at 700 °C for 12h under vacuum condition to obtain Ti metal. After that, the deuteration for this Ti sample was carried out under D_2 atmosphere of 1.0 MPa at 700 °C for 12h to obtain TiD_2. Then, the composite of TiD_2-$2LiBH_4$ was made by mechanical ball-milling method for 2 hours.

3.2 Fabrication of all-solid-state lithium ion batteries

The all-solid-state cells were fabricated by using the composite electrodes obtained above, $LiBH_4$ solid electrolyte, and lithium metallic disk. First of all, lithium metallic disk was put into a 16-mm-diameter-die, then it was covered with $LiBH_4$ powder and pressed together under 360 kg cm^{-2}. After that, the composite electrodes were introduced onto the $LiBH_4$ and pressed under 1450 kg cm^{-2} between current collectors made of stainless steel (SUS) to form layered structure in order of lithium metallic disk, $LiBH_4$, and the composite electrode as shown in Figure 3-2. This layered bulk was placed in the coin cells (2032 type, Hohsen Corp.) sealed with PFA gasket as shown in Figure 3-3.

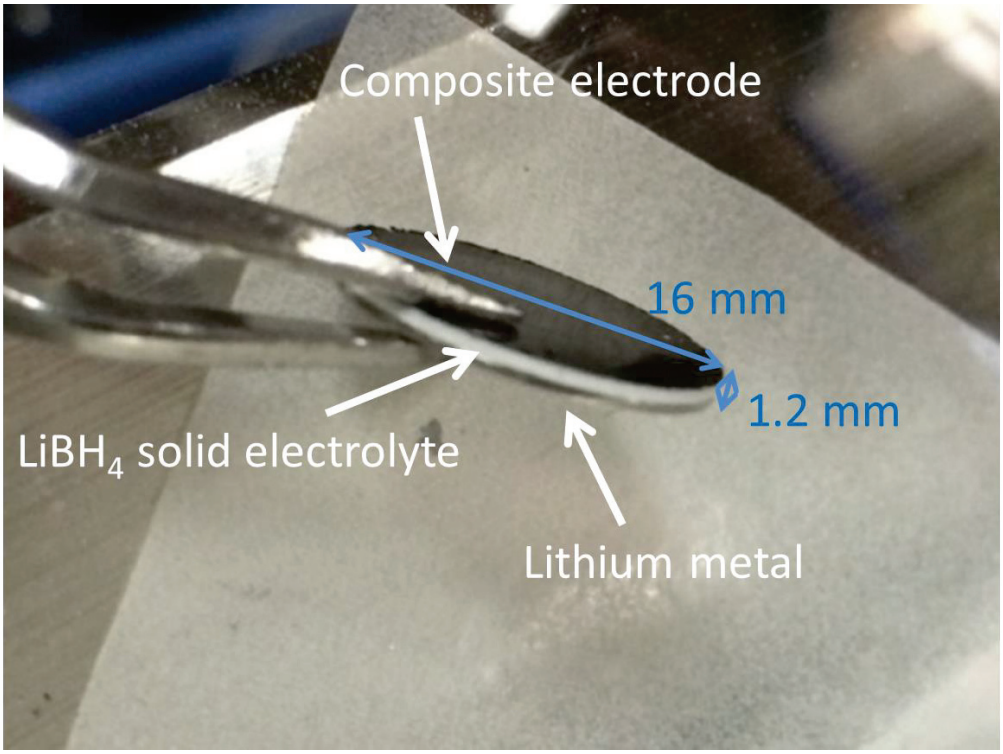

Figure 3-2 Picture of three layered bulk

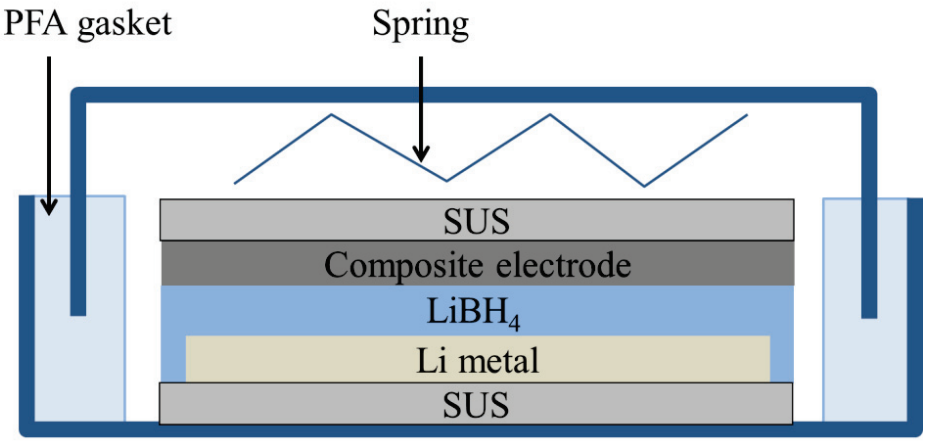

Figure 3-3 Schematic view of the coin cells

3.3 Electrochemical measurements by Chronopotentiometry

Chronopotentiometry is a method to measure the battery performance of electrode materials. The electrochemical test cells used in chronopotentiometry are composed of three types of electrodes, working electrode, counter electrode and reference electrode as shown in Figure 3-4. In the case of lithium ion batteries, lithium metal is used as both of counter and reference electrodes. Generally, to simplify the electrochemical test of the lithium ion batteries, counter electrode and reference electrode are connected to the same position as shown Figure 3-5, which is called two-electrode cell. With applying the constant current between working electrode and counter electrode, the time and potential of working electrode versus reference electrode are monitored. From the result, equilibrium potential of the charge-discharge reaction and specific capacity of the electrode materials are obtained. The specific capacity as a unit mAh g^{-1} of the electrode materials are calculated as follows,

$$Q = \frac{i \times t}{w}, \qquad (3\text{-}1)$$

where i is the applied current (mA), t is the time of charge-discharge (h) and w is the weight of active materials (g). The theoretical specific capacity is calculated as follows,

$$Q_{theoertical} = \frac{F \times n}{M}, \qquad (3\text{-}2)$$

where F is the Faraday constant (96500 $C \ \ mol^{-1}$ or A sec.mol^{-1}) , n is the number of electrons of the charge-discharge reaction and M is the formula weight of active materials ($g \ \ mol^{-1}$). For example, the theoretical specific capacity of graphite is calculated as follows,

$$96500[A \ \ sec.mol^{-1} \ ] \ \div 3600 \ [sec.h^{-1} \ ] \ \times 1000 \ [mA \ \ A^{-1} \ ] \div (12 \times 6) \ [g \ \ mol^{-1}] = 372 \ [mA \ \ g^{-1}] \ . \qquad (3\text{-}3)$$

One lithium ion per six carbons can be accommodated as the reaction of $6C + Li^+ + e^- \leftrightarrow C_6Li$. The specific capacity also can be calculated in volumetric capacity of mAh cm^{-3}. Both of specific and volumetric capacities are quite important factor for electrode materials to utilize for lithium ion batteries.

Procedure

In this work, the all-solid-state cells were fabricated in two electrode cell by using composite electrode and lithium metallic disc. The electrochemical performances were measured at 120°C in which the $LiBH_4$ solid electrolyte showed super ionic conductivity. In order to keep the temperature and prevent air exposure, oil bath was used as heat source.

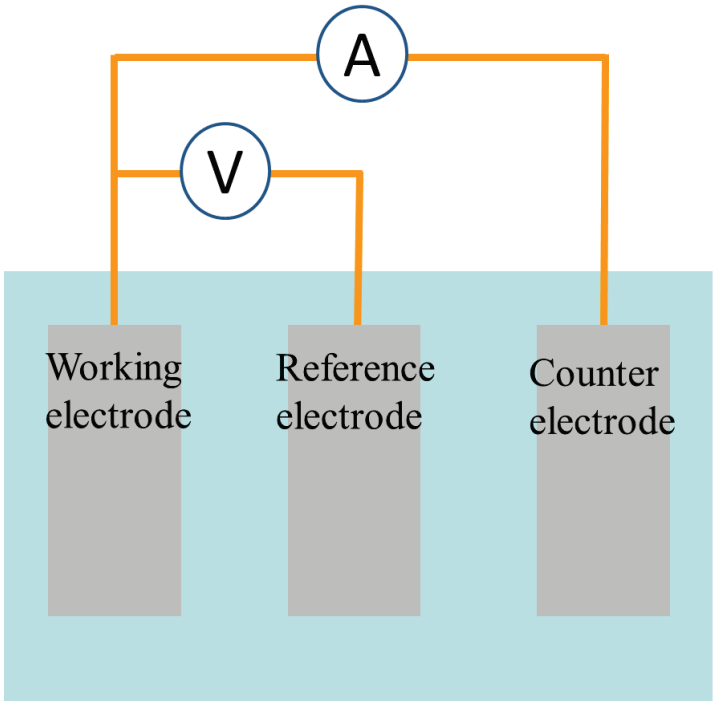

Figure 3-4 Schematic view of three-electrode cell

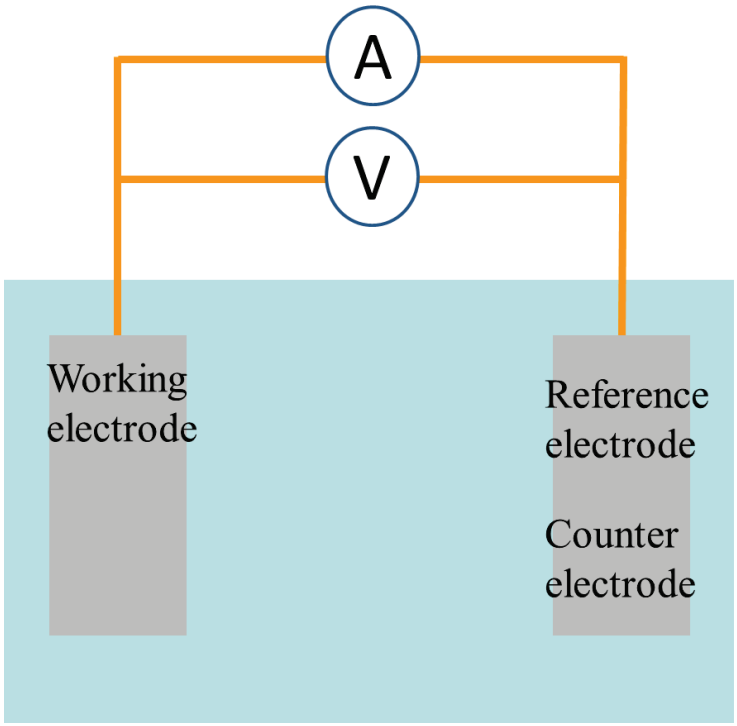

Figure 3-5 Schematic view of two-electrode cell

3.4 Characterization techniques

3.4.1 Powder X-ray diffraction (XRD) measurement

X-ray diffraction (XRD) is a technique that identifies the crystal structure of compounds. When an X-ray irradiate to a single crystal, the X-ray is scattered by electrons in atoms. As a result, the scattered X-rays show diffraction phenomenon when the following Bragg's law is satisfied,

$$2d_{hkl}\sin\theta = n\lambda, \qquad (3\text{-}4)$$

where *hkl* are Miller indexes, d_{hkl} is the distance between the corresponding planes and λ is the wavelength of the beam. When the compounds are powdered, the randomly-located fine crystals show Debye-Scherrer ring as shown in Figure 3-6 [3-3]. Since the satisfaction depend on the crystal structure of the materials, the information of the structure can be obtained by analyzing the diffraction patterns, then the material can be identified.

Procedure

In this work, powder XRD measurement (RINT-2100, Rigaku) was performed to identify the state-of-charge of the electrode materials by using Cu-Kα radiation at room temperature. Since the XRD profiles of the electrode materials depend on the lithiation yield, the state-of-charge can be identified by analyzing the profiles. The XRD

measurement was performed after the all-solid-state cell was opened at the required potentials and the composite electrode was disassembled from the cell. This electrode material was put onto the glass plate covered with poly-imide film (Kaptom, DuPont-Toray Co., LTD.) sealed with high vacuum grease (Apiezon Grease, M&I Material Ltd.) for the XRD measurement.

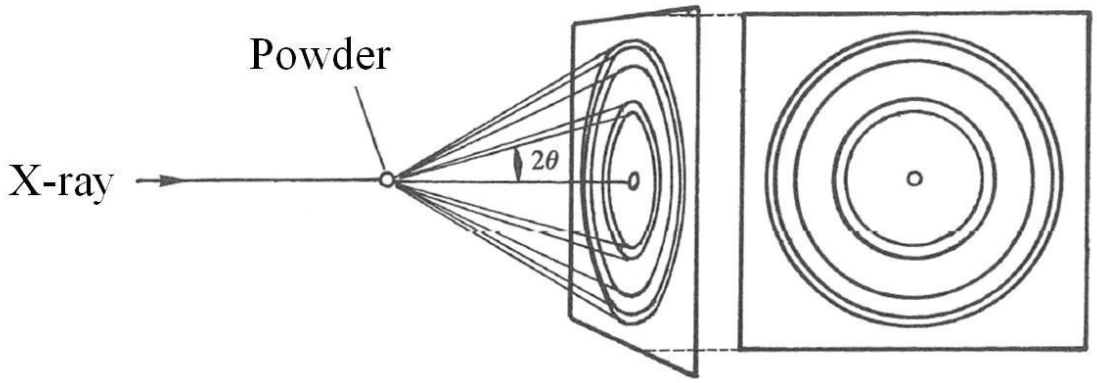

Figure 3-6 Aspect of powder X-ray diffraction measurement [3-3]

3.4.2 X-ray photoelectron spectroscopy (XPS)

X-ray photoelectron spectroscopy (XPS) is a surface analysis technique that identifies the elemental composition of the compounds, and their chemical state and electronic state. This measurement is based on photoelectric effect. When materials are irradiated under high vacuum condition by an X-ray with higher energy than binding energy of electrons, the electrons are ejected from their core level. Then, the kinetic energy of emitted electrons is analyzed by electron spectrometer. While the X-ray penetrate into the compounds deeply, the escape depth of the electrons is in nanometer order as shown in Figure 3-7 [3-4]. In other words, only surface information can be obtained by analyzing the ejected electrons. Since the kinetic energy of the ejected electrons depends on the energy of incident X-ray, the binding energy of the electrons can be identified as follows,

$$E_B = h\upsilon - E_K - W, \qquad (3\text{-}5)$$

where $h\upsilon$ is the incident energy of the photon, E_K is the kinetic energy of the electron, and W is the spectrometer work function. Usually, Mg-Kα (1253.6 eV) or Al-Kα (1486.6 eV) is used as X-ray source due to the narrow natural width of the energy which determines the limit of resolution. The schematic diagram of the XPS process is shown in Figure 3-8, where an electron from the K shell is ejected from the atom [3-5]. Since each element has characteristic binding energy associated with each core atomic orbital, the elements that exist in the surface can be identified. In addition, the exact binding

energy often has a “chemical shift”. For example, higher oxidation state shows a higher binding energy due to the extra coulombic interaction between electrons and the nucleus. Therefore, the chemical shift exhibits the chemical state and electronic state, and supports the identification of the compounds. When taking the chemical shift into consideration, it is important to give attention to electrostatic charging. Photoemission from an insulating sample causes electrostatic charging to occur in the positive direction. As a result, a peak position shift is observed in the direction of higher binding energy. Therefore, when charge compensation is necessary, the low-energy electron beam is used, leading to the neutralization to their correct position during data processing.

For the XPS measurement, ultra-high vacuum condition of 10^{-8} to 10^{-10} Pa is required because the analytical signal of low energy electrons is easily scattered by the residual gas molecules and the residual gas is easily adsorbed onto a solid surface of samples. To realize such an ultra-high vacuum condition, generally, rotary pumps as primary pump and turbomolecular pumps as secondary pump are used.

Procedure

In this work, XPS measurement (ESCALAB 250Xi, Thermo Fisher Scientific) was performed to analyze the surface state of the electrode materials by using Al-Kα radiation at room temperature. Since it is well known that some by-products often generate on the surface of electrode materials during the charge-discharge process and have an effect on electrochemical properties, it is important to analyze the surface state of electrode

materials. The XPS measurements were performed after the all-solid-state cell was opened at the required potentials and the composite electrode was disassembled from the cell. Since the solid electrolyte is insulator and is also included in the composite electrode, the low-energy electron beam was used in order to prevent electrostatic charging.

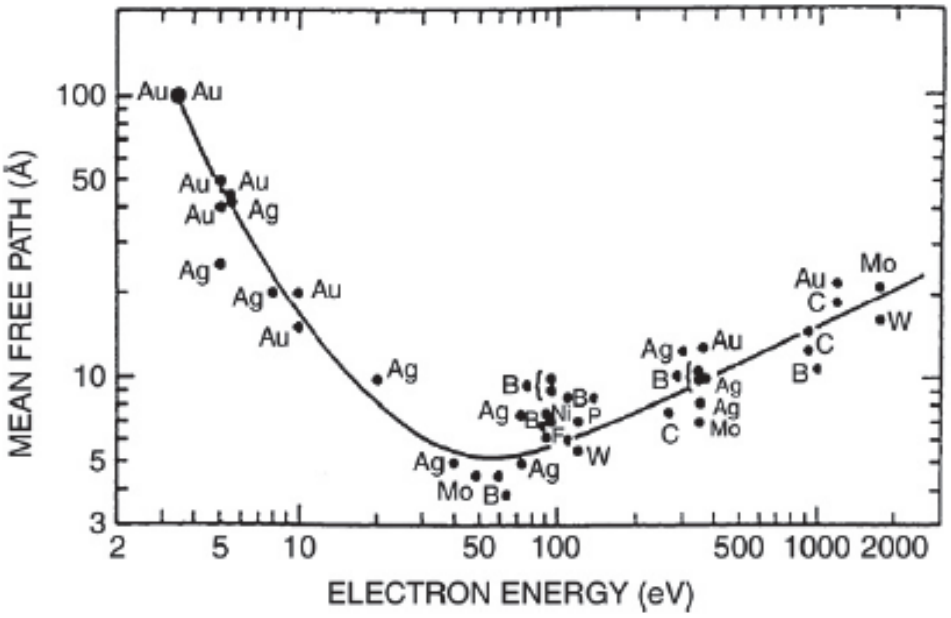

Figure 3-6 Mean-free-path of electrons as a function of energy [3-4]

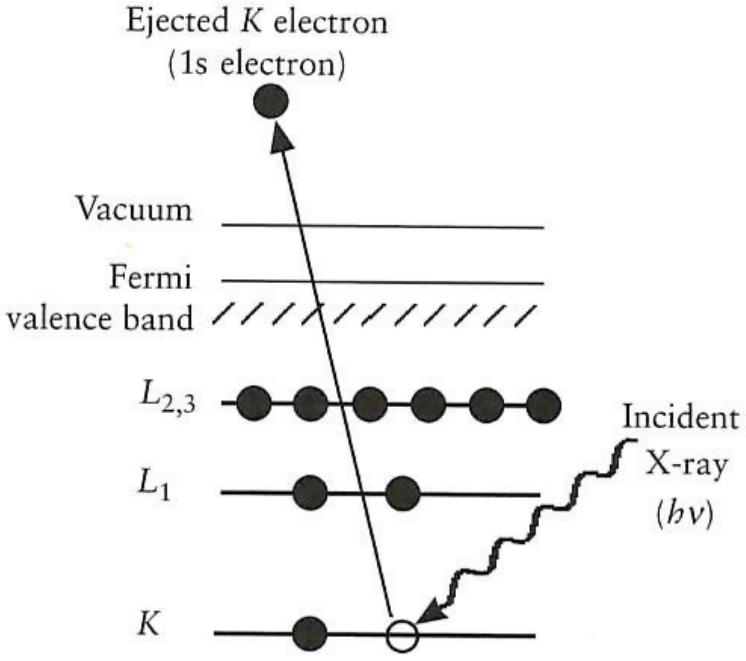

Figure 3-7 Schematic of the XPS process [3-5]

3.4.3 Fourier transform infrared (FT-IR) spectroscopy

Fourier transform infrared (FT-IR) spectroscopy is a technique that identifies the presence of certain functional groups in molecules. In this technique, materials are irradiated by white infrared light whose wavelength is ranged from 10 to 15,000 cm^{-1}. Since the energy of infrared region matches the energy of molecular vibration, the molecules absorb specific frequencies corresponding to the vibration state. Thus, infrared absorption spectra show information about the binding state of the atoms that constitute a molecule, in other words, the functional groups.

Although a molecule can vibrate in many ways, all vibrational modes do not show IR absorption phenomenon. For a vibrational mode of the molecule to be IR active, it is necessary for dipole moment to change during the vibration. As an example, the vibration modes of carbon dioxides (CO_2) are shown in Figure 3-8. The symmetric stretching vibration mode (ν_1) in CO_2 is not IR active since the dipole moment is not changed. On the other hand, in the case of asymmetry vibration (ν_2) mode and bending vibration mode (ν_3), dipole moment is changed by the vibration mode, therefore the two vibration modes are IR active.

In the vibrational spectroscopy, isotope labeling is often used due to the fact that isotopically substituted molecule shows different behavior than unsubstituted molecule for the absorption frequency. In order to understand the effect of isotope labeling, a simple spring model is introduced as shown in Figure 3-9. Regarding the motional state, the frequency of the vibration is expressed by “Hooke’s law” as follows,

$$\nu = \frac{1}{2\pi}\sqrt{\frac{k}{\mu}}, \quad (3\text{-}6)$$

$$\mu = \frac{m_1 m_2}{m_1 + m_2}, \quad (3\text{-}7)$$

where ν is frequency, m_1 and m_2 are mass of each atom, k is the force constant, and μ is effective mass. When the atom in a molecule is changed to heavy isotope, the IR absorption peak is shifted to lower energy than that of the unsubstituted molecule, because μ is larger than that of unsubstituted molecule. By using the isotope labeling technique, it can be realized to track the pathway through the chemical reraction.

Procedure

In this work, Fourier transform infrared (FT-IR) spectroscopy measurement (Spectrum One Perkin-Elmer) was performed by using a diffuse reflection cell to investigate the IR active stretching modes of the functional groups such as B-D bonds in the solid powder sample. The sample was diluted by KBr with a mass ratio of 1:10 (sample : KBr) and placed into Al pan. Then, the Al pan was introduced into the diffusion reflection cell with KBr window, then the mesurement was started.

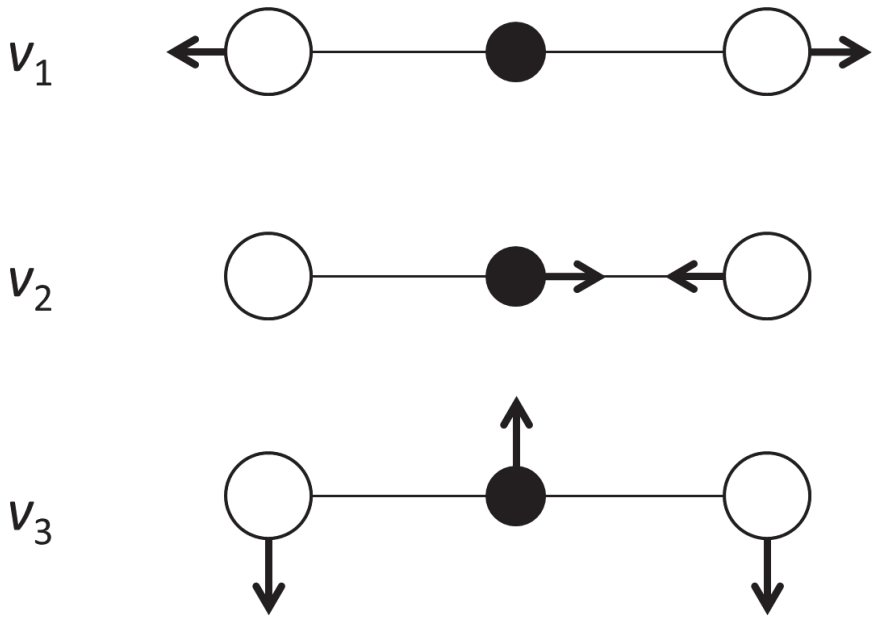

Figure 3-8 Vibration modes for CO_2

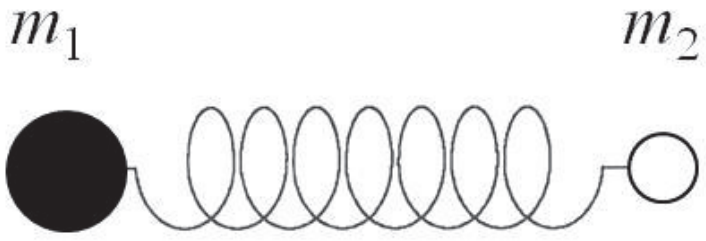

Figure 3-9 Schematic view of stretching vibration for diatomic molecule

[3-1] Y. Oumellal, W. Zaidi, J.P. Bonnet, F. Cuevas, M. Latroche, J. Zhang, J.L. Bobet, A. Rougier, L. Aymard, Int. J. Hydrogen Energy, 37 (2012) 7831-7835.

[3-2] S. Ikeda, T. Ichikawa, K. Kawahito, K. Hirabayashi, H. Miyaoka, Y. Kojima, Chem. Commun., 49 (2013) 7174-7176.

[3-3] S. Lesley, M. Elaine, SOLID STATE CHEMISTY (Japanese translation), ed.R. Sone, K. Komoto, K. Hirao, (2006).

[3-4] S.J. Rosenthal, J. McBride, S.J. Pennycook, L.C. Feldman, Surf. Sci. Rep., 62 (2007) 111-157.

[3-5] J.F. Watts, J. Wolstenholme, An Introduction to Surface Analysis by XPS and AES, Wiley, 2003.

4 Results and discussion

4.1 MgH_2 system

4.1.1 Initial charge-discharge properties of MgH_2 conversion reaction

Figure 4-1 showed the initial charge-discharge curves of the MgH_2 electrode between 2.0 V and 0.05 V using $LiBH_4$ solid electrolyte under the current density of 400 mA g^{-1} at 120 °C. The Li insertion curve immediately reached 0.5 V and showed distinctive flat plateau corresponding to MgH_2 conversion reaction ($MgH_2 + 2Li^+ + 2e^- \rightarrow Mg + 2LiH$) [4-1], where the plateau voltage was almost the same level as theoretical value (0.52 V vs. Li^+/Li). Then, the curve showed plateau at around 0.1 V corresponding to alloying reaction ($xMg + yLi^+ + ye^- \rightarrow Li_yMg_x$) and the whole initial Li insertion capacity was 2405 mAh g^{-1}. In the Li extraction curve, the plateaus corresponding to de-lithiation process of MgH_2 conversion reaction and de-alloying reaction from Li_yMg_x were observed at slightly higher voltages than 0.5 V and 0.2 V, respectively. Then, surprisingly, the whole Li extraction curve showed quite high capacity of 2791 mAh g^{-1} with the 116% coulombic efficiency, which exceeded a capacity expected from the Li insertion amount. From the feature of the Li extraction curve, it was considered that a side-reaction occurred as seen on the plateau at 1.2 V which was not observed in the Li insertion curve.

In order to identify the electrochemical reaction, ex-situ XRD measurement was performed at the different states-of-charge as shown in Figure 4-2, where the roman numbers (i) ~ (vi) correspond to states-of-charge shown in Fig. 4-1. It is noteworthy that all the profiles contain peaks corresponding to $LiBH_4$ of solid electrolyte. At the initial

state (i), the broad peaks corresponding to MgH_2 were observed since the composite electrode was prepared by ball milling treatment. After Li insertion, the broad peaks were disappeared and the peaks corresponding to the Mg and LiH were generated (ii), indicating that MgH_2 reacted with Li ions electrochemically and transformed into Mg and LiH. With further lithiation, it was observed that the Mg turned into the alloying state of Li_3Mg_7 (iii). For the Li extraction processes, Li_3Mg_7 changed back to Mg, and then as shown in Figs. 4-2 (iv, v), MgH_2 peaks were reappeared and the generated peaks were quite sharp compared with the peaks before Li insertion. It was noted that the XRD profile showed new peaks corresponding to α-$Mg(BH_4)_2$ at the voltage reached up to 2 V as shown in Fig. 4-2 (vi). From this result, it was expected that the plateau around 1.2 V could be due to the conversion reaction related to α-$Mg(BH_4)_2$ as follows,

$$Mg + 2LiBH_4 \rightarrow Mg(BH_4)_2 + 2Li^+ + 2e^- \qquad (4\text{-}1)$$

Furthermore, generation of the dual-cation borohydride, for example, $Li_{1-x}Mg_{1-y}(BH_4)_{3-x-2y}$ is possibly occurring as is proposed in the previous reported works [4-2, 3]. Actually, Bardají et al. claimed that a small amount of $LiBH_4$ can be dissolved into $Mg(BH_4)_2$ and this solid solution showed similar XRD pattern to α-$Mg(BH_4)_2$. In case of this electrochemical reaction, it is reasonable to suppose that the dual-cation borohydride exists as an intermediated state.

The surface chemical structure of MgH_2–$LiBH_4$ composite electrode was investigated

by XPS. Figure 4-3(a) showed B1s spectra of the composite electrode, where the roman numbers (i), (iii) and (vi) correspond to states-of-charge shown in Fig. 4-1. The initial state of the composite electrode (i), two peaks with binding energy positioned at 191.6 eV and 187.7 eV were observed, which were attributed to B_2O_3 and $LiBH_4$, respectively. It is considered that the B_2O_3 was included as impurity. After lithium insertion (iii), the same spectrum as the initial state of the composite electrode was observed, indicating that the lithium insertion process stably occurred with no side-reaction. Generally, some products of solid-electrolyte-interface (SEI) caused by a side-reaction, e.g. LiF, Li_2CO_3, were observed after the lithium insertion process in conventional liquid electrolyte system [4-4]. Additionally, the SEI often gave negative effect on cyclability, rate capability and so on. In terms of this point, it was expected that this system had better electrochemical properties because it had the stable electrode-electrolyte interface. After lithium extraction process (vi), a new peak with binding energy located 192.4 eV was observed. It was considered that the peak could be assigned to $Mg(BH_4)_2$ in view of the XRD results of Fig. 4-2.

Figure 4-3 (b) showed the Mg2s spectra of MgH_2–$LiBH_4$ composite electrode. The spectrum of initial state (i) showed only one broad peak at 88.7 eV corresponding to active material of MgH_2 and impurity of Mg. After lithium insertion process (iii), the only peak was observed at the same position as the initial state with quite low intensity [4-5]. From the XRD results of Fig. 4-2, it was expected that the peak included Li-Mg alloy in addition to MgH_2 and Mg. The decrease of intensity might be due to the morphology of

electrochemical products. It was considered that the MgH_2 transformed into Mg covered with LiH after the lithiation, meaning that LiH interrupted the electrons generated from Mg surface. After lithium extraction process (vi), the peak was observed at 89.7 eV slightly higher value than MgH_2. In view of XRD results of Fig. 4-2, the peak could be attributed to $Mg(BH_4)_2$.

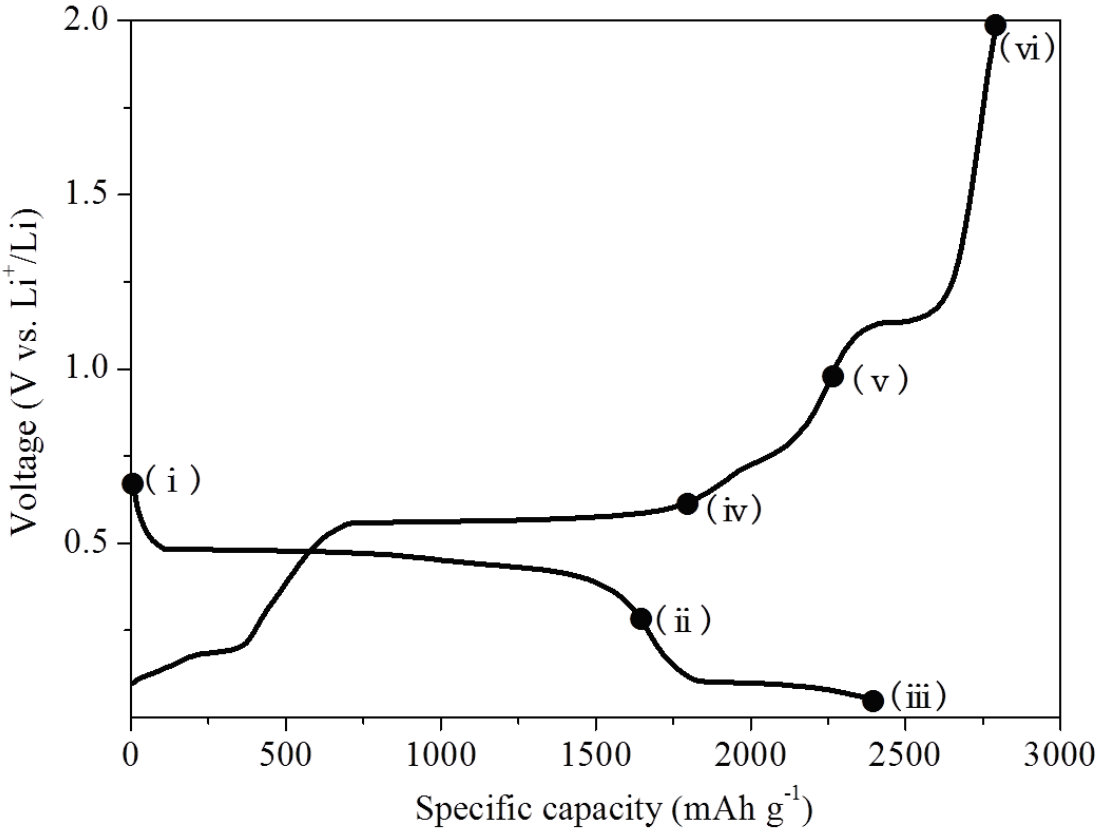

Figure 4-1 The first galvanostatic charge–discharge curves for MgH_2-$LiBH_4$ electrode in the voltage range of 2.0 V – 0.05 V at a current density of 400 mAh g^{-1} at 120°C

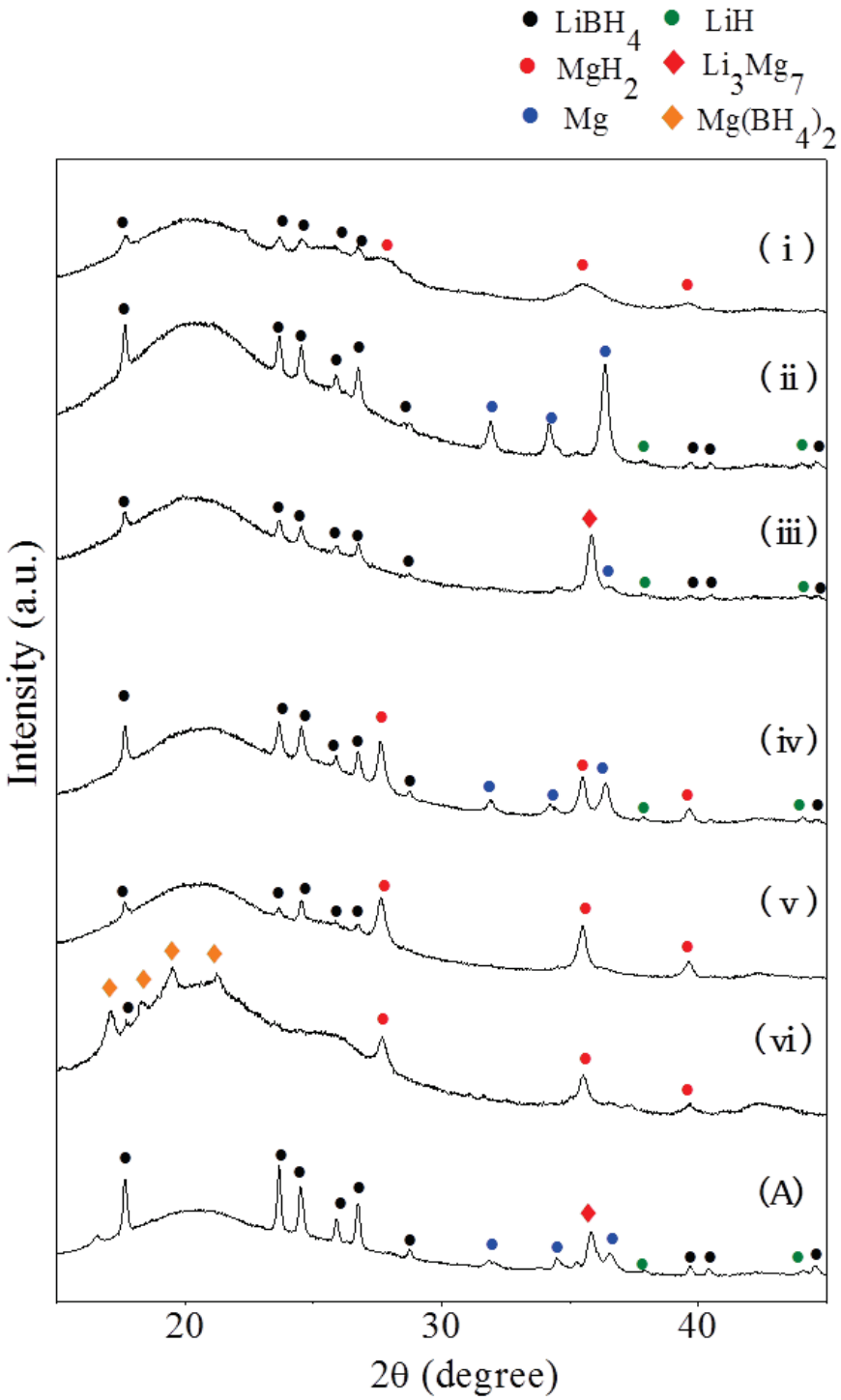

Figure 4-2 Ex-situ XRD patterns of MgH_2-$LiBH_4$ at the various states-of-charge

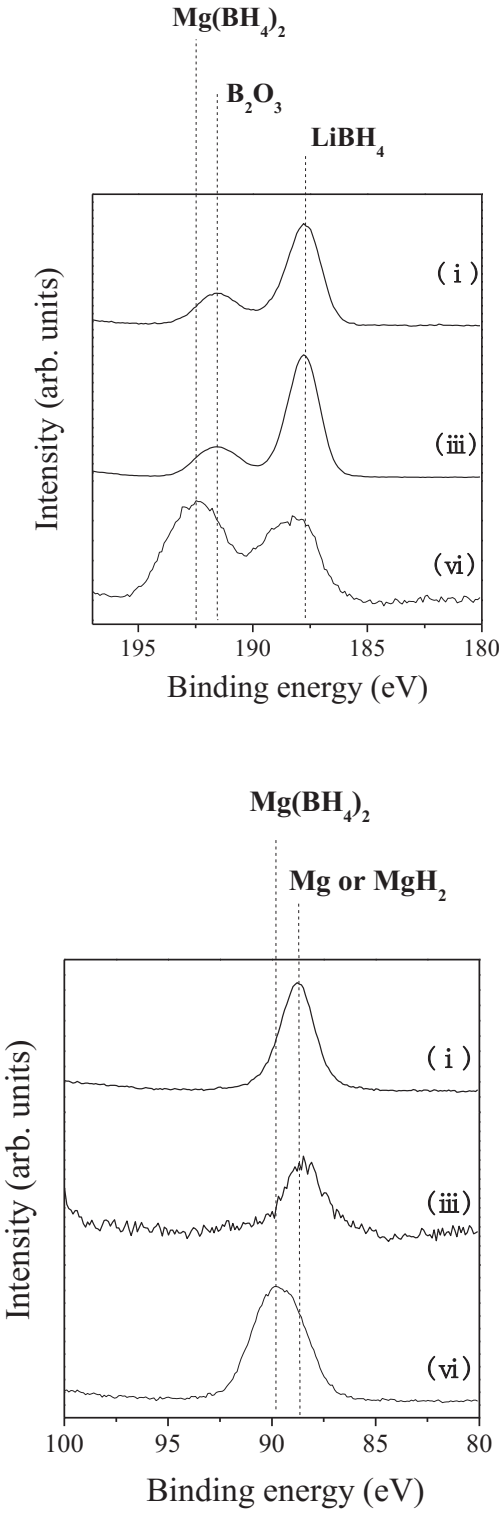

Figure 4-3 XPS spectra of MgH_2-$LiBH_4$ at the various states-of-charge (a) B1s, and (b) Mg2s

4.1.2 Cycle properties of MgH_2 conversion reaction

Considering the results of XRD and XPS, the MgH_2 composite electrode exhibited electrochemical reaction of MgH_2 conversion reaction (0.5 V vs. Li^+/Li), Li-Mg alloying reaction (0.1 V vs. Li^+/Li) and $Mg(BH_4)_2$ conversion reaction (1.2 V vs. Li^+/Li). In order to investigate the cyclability of these electrochemical reactions, charge-discharge measurements were performed with controlling working voltage windows. Cyclic properties of MgH_2 composite electrode in the different voltage windows were shown in Figure 4-4 to 4-6. As shown in Fig. 4-4 (a) for the voltage window between 2.0 – 0.05 V, new plateau on discharge profile was observed at 0.8 V from the second cycle. The plateau could be assigned to the lithiation process of $Mg(BH_4)_2$: ($Mg(BH_4)_2 + 2Li^+ + 2e^- \rightarrow Mg + 2LiBH_4$), which is the reverse direction of Equation (4-1), because it was confirmed that the XRD profile of the lithiated state of the second cycle showed no peaks corresponding to $Mg(BH_4)_2$ as shown in Fig. 4-2 (A). In other words, $Mg(BH_4)_2$ can be formed and vanished during the charge-discharge processes, indicating that the generation of $Mg(BH_4)_2$ is electrochemically reversible. However, it was considered that the $Mg(BH_4)_2$ is easily inactivated because the plateau was gradually shortened and disappeared after only 20 cycles. Although this system showed high Li insertion capacity of 2791 mAh g^{-1} at the 1st cycle and 734 mAh g^{-1} at the 50th cycle, the initial capacity retention ratio after 50th cycle was 30% with unstable coulomb efficiency as shown in Fig. 4-4 (b). Therefore, it is concluded that this side-reaction corresponding to the formation of $Mg(BH_4)_2$ has an adverse effect for the cycle properties.

In order to obtain much better cycle properties, the working voltage window was limited to 1.0 – 0.05 V to avoid the side-reaction corresponding to reaction (1) as shown in Fig. 4-5 (a). It can be seen that a reversible capacity of 2308 mAh g^{-1} was obtained in the first cycle, which was slightly lower value than the case of 2.0 – 0.05 V. The Li insertion curves showed no plateau at 0.8 V even after several cycles, indicating $Mg(BH_4)_2$ was not formed during the Li extraction process below 1.0 V. The plateau at 0.2 V in the charging process should be caused by the de-lithiation from the Li-Mg alloy : ($Li_yMg_x \rightarrow xMg + yLi^+ + ye^-$) as mentioned above. Another point to be noticed is that the plateau at 0.75 V on the Li extraction process was found, becoming clear in the increasing cyclic number up to 10^{th} cycle. It could be caused by Mg generated by the de-lithiation from the Li-Mg alloy, meaning that two different Mg particles, which were generated from MgH_2 and Li-Mg alloy, showed different Li extraction plateaus. Actually, Mg from the Li-Mg alloy could have a difficulty to react with LiH and caused relatively high plateau voltage. After the initial cycles, the discharge capacity slightly increased as shown in Fig. 4-5 (b). This phenomenon could be explained by an inhomogeneous or local distribution of active material in the initial cycles. That is to say, some part of unreacted active materials could join electrochemical reaction in a later cycle. In the case for the limited voltage window of 1.0 – 0.05 V as shown in fig. 4-5(b), this system showed that the initial capacity retention ratio after 50^{th} cycle was 53%, meaning that it was more moderate capacity fading compared with the case of the voltage window between 2.0 – 0.05 V, which includes $Mg(BH_4)_2$ conversion reaction. Although the electrode capacity

remained 1261 mAh g^{-1} after 50 cycles with nearly 100% coulombic efficiency, the existing of Li-Mg alloy showed unfavorable high and low plateau voltages at 0.75 V and 0.2 V on the Li extraction process.

To further improve the cyclic performance, the lower working voltage was limited to 0.3 V to avoid the process of Li-Mg alloying reaction as shown in Fig. 4-6 (a). The profile exhibited the plateau of only MgH_2 conversion reaction around 0.5 V and showed initial reversible capacity of 1487 mAh g^{-1}. Surprisingly, the voltage difference between charge (Li extraction)-discharge (Li insertion) and was only 0.05 V, which is much smaller than that of the MgH_2 electrodes working with a liquid electrolyte system [4-1]. It is worthy noticed that the plateaus at 0.75 V and 0.2 V shown in Fig. 4-5 (a) on the Li extraction curve was not observed since the Li-Mg alloy was not generated for the lithiation process above 0.3 V. Although the gradual capacity fading was confirmed in the initial several cycles, the capacity degradation almost stopped after 13 cycles and showed 963 mAh g^{-1} after 50 cycles as shown in Fig. 4-6 (b). The initial capacity retention ratio after 50^{th} cycle was 62%. This result suggests the MgH_2 electrode works properly between 1.0 V and 0.3 V without any side reactions during the battery operation. Although the total capacity was decreased by narrowing the working voltage windows, it showed quite stable capacity curve.

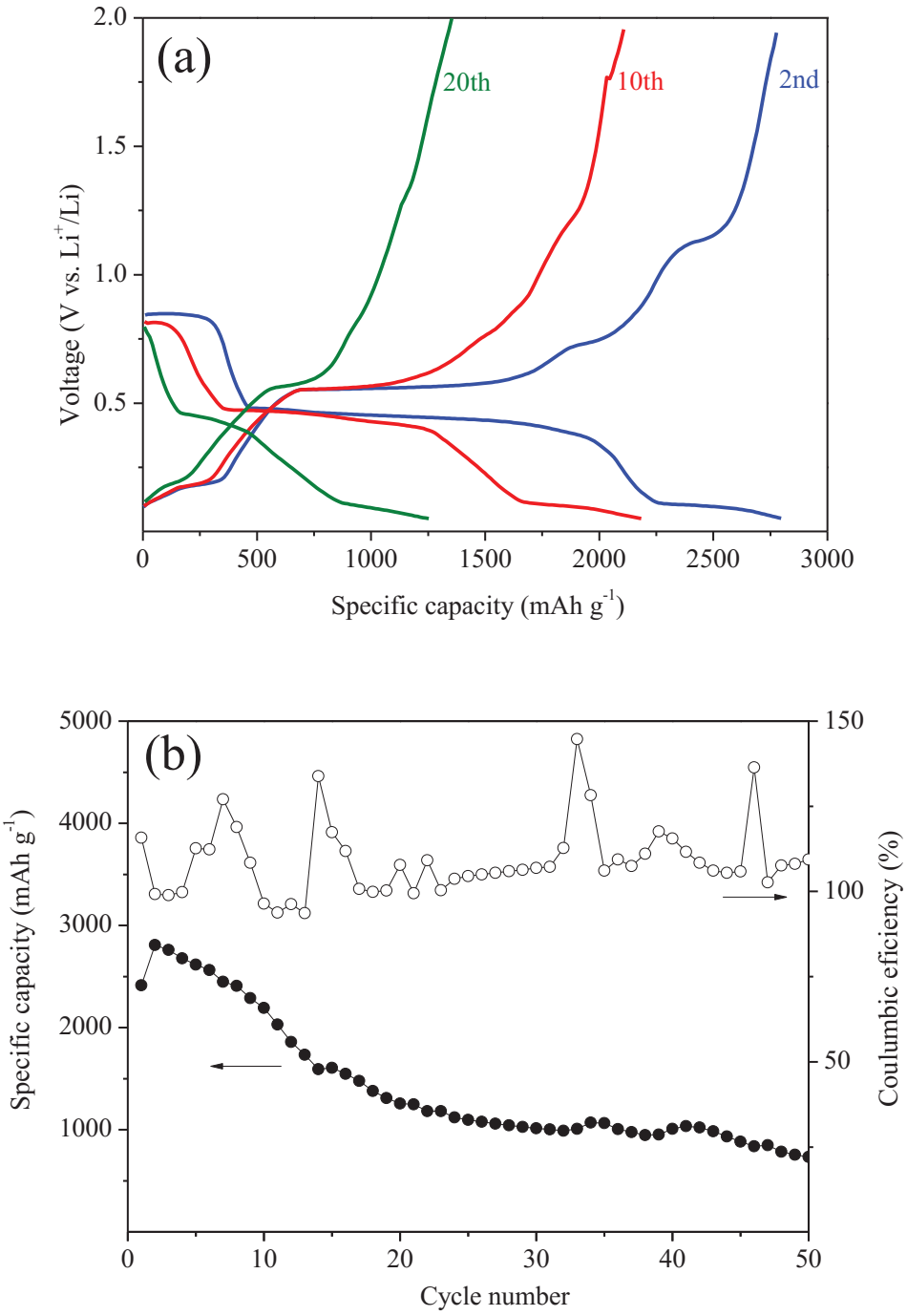

Figure 4-4 Cyclic performances of the MgH_2–$LiBH_4$ composite electrode in the voltage range of 2.0 – 0.05 V at a current density of 400 mA g^{-1} at 120°C (a), and the cyclic stability curves of the MgH_2–$LiBH_4$ composite electrode (b)

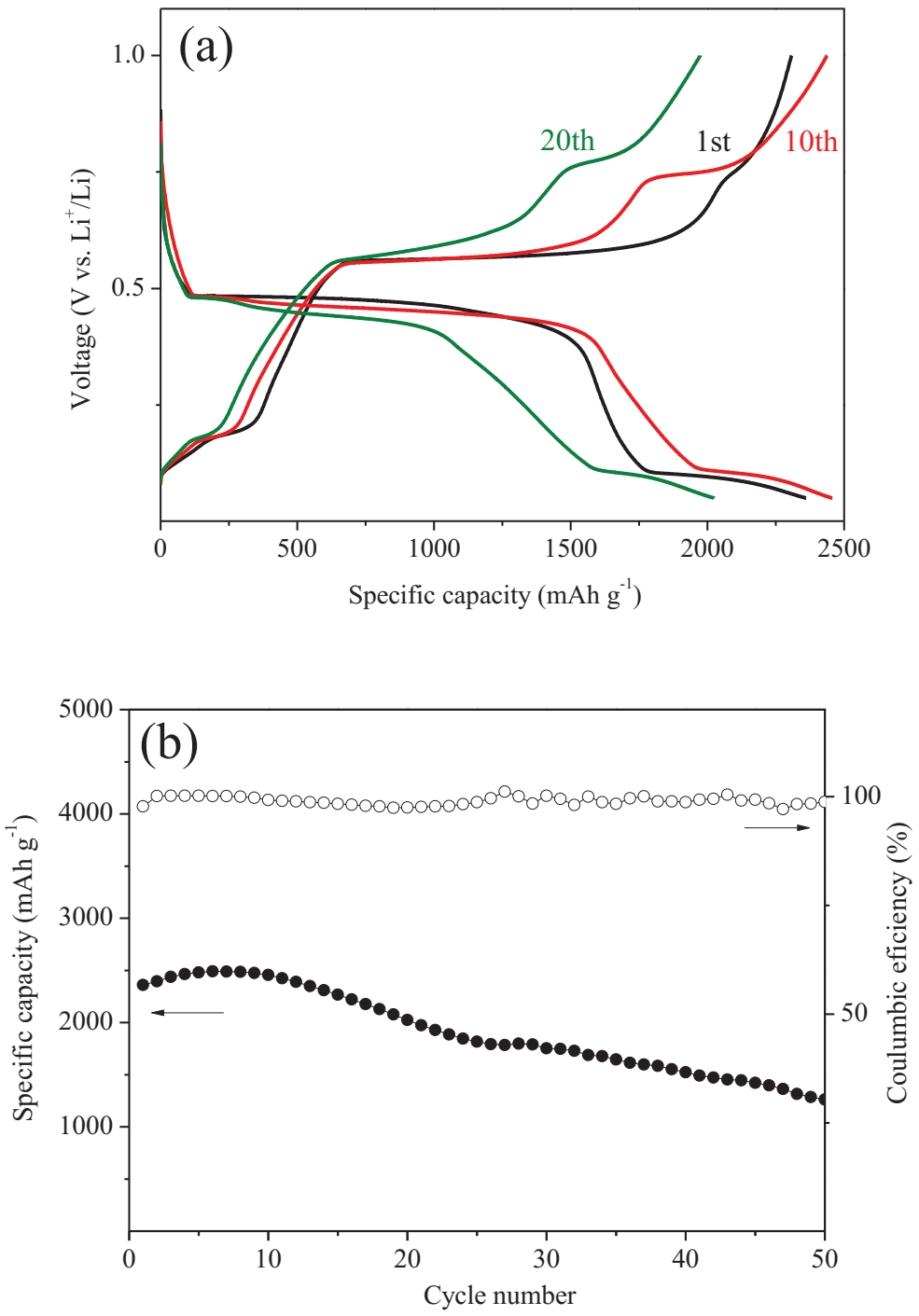

Figure 4-5 Cyclic performances of the MgH_2–$LiBH_4$ composite electrode in the voltage range of 1.0 – 0.05 V at a current density of 400 mA g^{-1} at 120°C (a), and the cyclic stability curves of the MgH_2–$LiBH_4$ composite electrode (b)

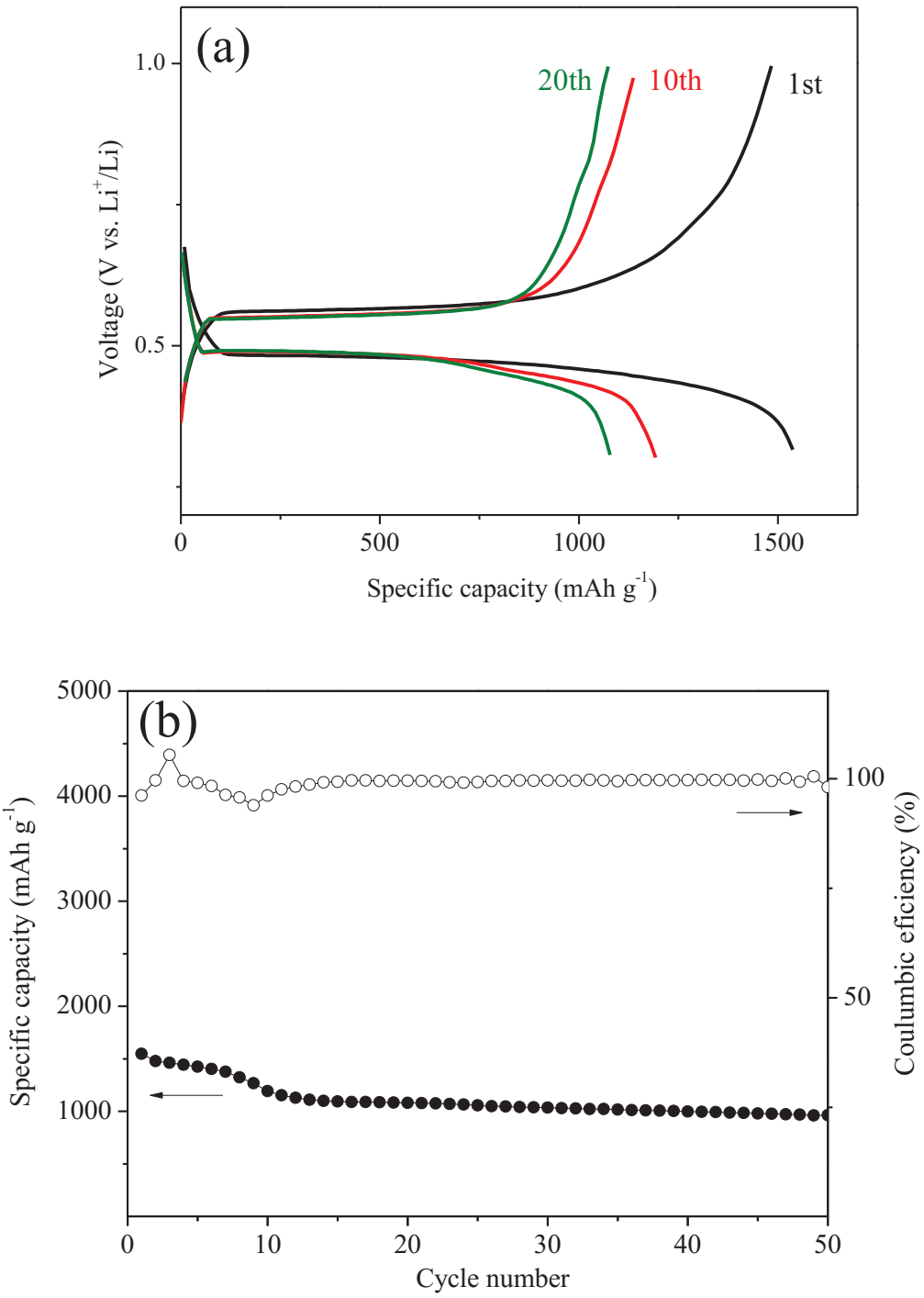

Figure 4-6 Cyclic performances of the MgH_2–$LiBH_4$ composite electrode in the voltage range of 1.0 – 0.3 V at a current density of 400 mA g^{-1} at 120°C (a), and the cyclic stability curves of the MgH_2–$LiBH_4$ composite electrode (b)

4.1.3 Summary

In this work, MgH_2 was performed as a negative electrode material for lithium ion batteries by using $LiBH_4$ solid electrolyte. $LiBH_4$ acts as a multifunctional ion conductor and promotes not only Li^+ but also H^- conductivity, resulting in a much higher reversibility for the hydride conversion reaction. Furthermore, the detailed reaction processes during discharge-charge and the cyclic properties had been investigated. It showed not only MgH_2 conversion reaction at 0.5 V vs. Li^+/Li but also conversion reaction of $Mg(BH_4)_2$ between 0.8 – 1.2 V vs. Li^+/Li and Li-Mg alloying reaction at 0.1 V vs. Li^+/Li. Although the total capacity was decreased by narrowing the working voltage windows, the capacity retention ratio was improved and showed quite stable coulombic efficiency.

Interestingly enough, $Mg(BH_4)_2$ showed electrochemically reversible conversion reaction in lithium ion batteries. Although the capacity retention is too poor at present, this result represents a possibility that complex metal hydrides ($LiNH_2$, $Mg(NH_2)_2$, etc.) can also act as negative electrode materials for lithium ion batteries.

4.2 TiH_2 system

4.2.1 Hydrogen exchange effect of TiH_2-$LiBH_4$ composite

In the section of MgH_2 system, it was observed that electrochemical properties of MgH_2 were improved by using $LiBH_4$ solid electrolyte. As one of the possible reasons, it was considered that the mobility of H^- in MgH_2 was enhanced by $LiBH_4$. Focused on the phenomenon, the $LiBH_4$ solid electrolyte was applied to TiH_2 electrode.

First of all, TiD_2 was synthesized to investigate the hydrogen exchange effect between TiH_2 and $LiBH_4$. Figure 4-7 (a) showed the XRD profile of pristine TiH_2 (as prepared). The clear peaks corresponding to TiH_2 were observed. For the product after the dehydrogenation treatment at 700°C for 12h, the diffraction pattern corresponding to Ti was observed as shown in Figure 4-7 (b). After that, the deuteration for this Ti sample was carried out under D_2 atmosphere of 1.0 MPa at 700 °C for 12h. As shown Figure 4-7 (c), the peaks corresponding to Ti were completely disappeared, and the peaks corresponding to TiD_2 and $TiC_{0.5}D_{0.707}$ were observed. The reason for the formation of $TiC_{0.5}D_{0.707}$ was considered that some carbon species was included as impurity in the pristine TiH_2 and reacted with Ti and D_2. Then, the obtained deuteride material was ball milled with $LiBH_4$ for 2h to synthesize TiD_2-$LiBH_4$ composite.

Figure 4-8 showed the results of in-situ IR spectroscopy for TiD_2-$LiBH_4$ composite. At room temperature, the peaks corresponding to B-H stretching vibration (2280 cm^{-1}) and H-O-H bending vibration (1660 cm^{-1}) were observed. It was considered that the H-O-H bending was due to the adsorbed H_2O, therefore, the peak gradually disappeared with an

increasing temperature. Meanwhile, the peak of the B-D stretching vibration (1688 cm^{-1}) was found at 50°C, and this peak was slightly increased with the increasing temperature. This result indicated that H atoms of $[BH_4]^-$ anions were exchanged for D atoms in TiD_2. The hydrogen exchange effect was observed not only MgH_2-$LiBH_4$ composite [4-6] but also TiH_2-$LiBH_4$ composite.

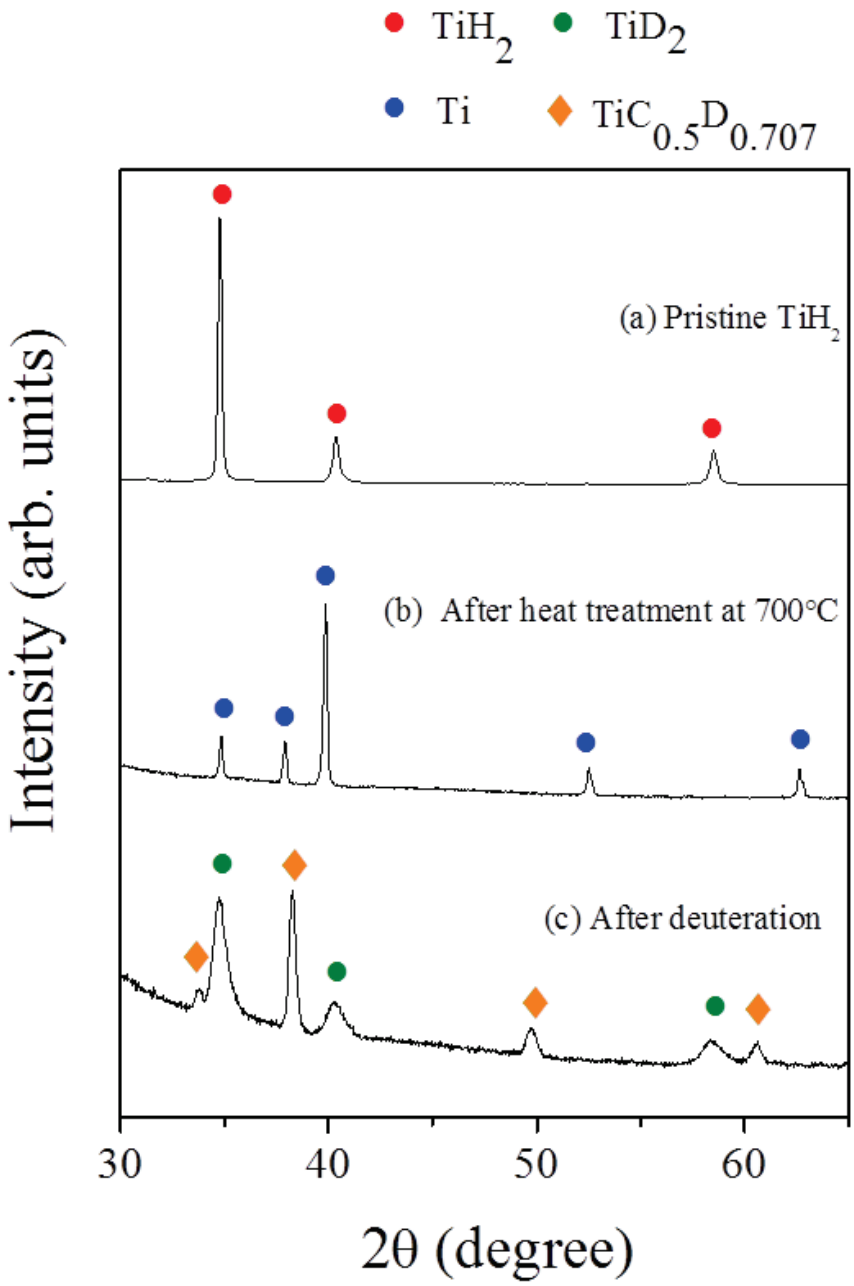

Figure 4-7 XRD profiles of pristine TiH_2 (a), TiH_2 after heat treatment at 700 °C (b), deuteration sample (c)

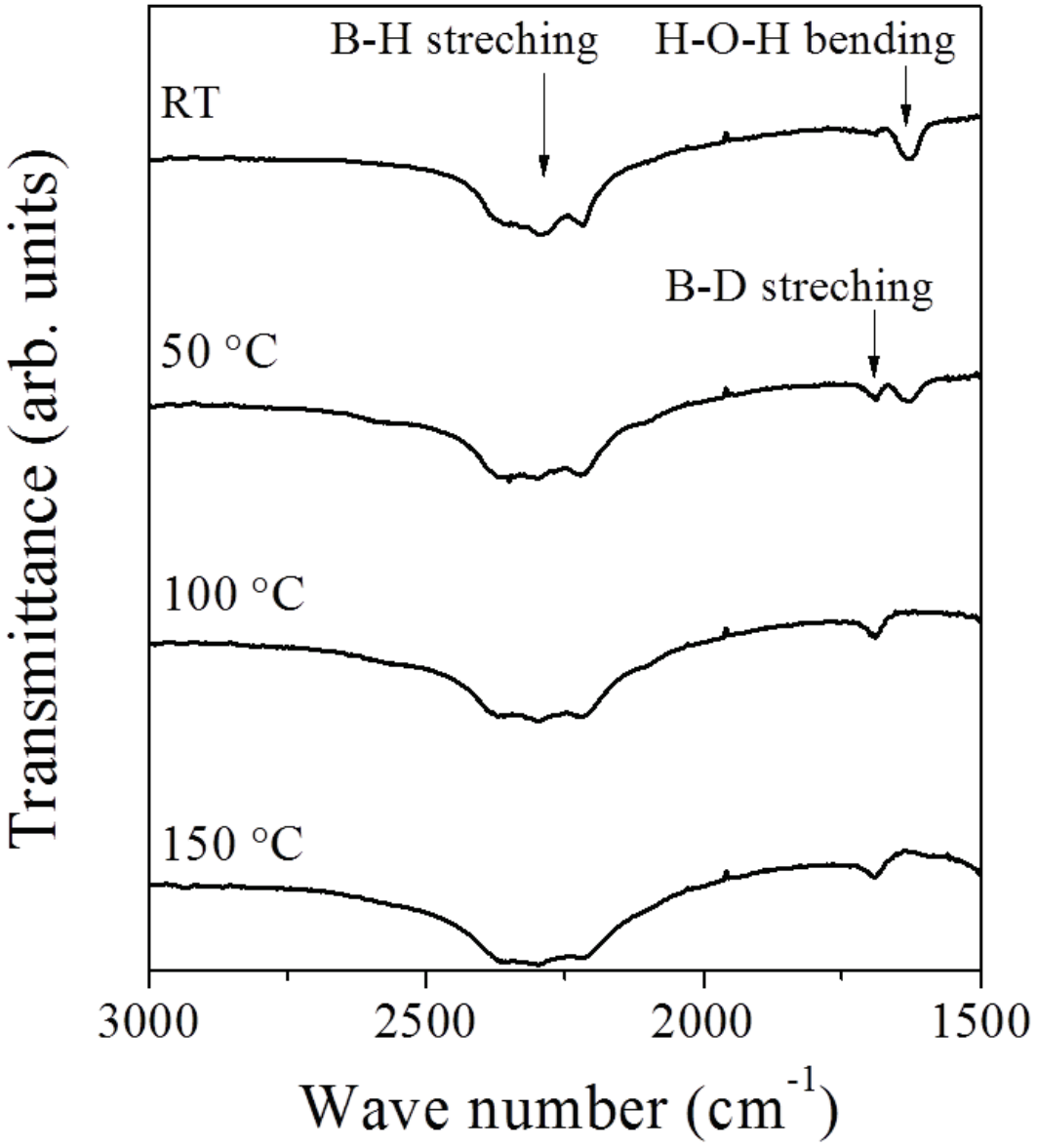

Figure 4-8 In-situ FT-IR spectra of TiH_2-$LiBH_4$ composite

4.2.2 Charge-discharge properties of TiH_2 conversion reaction

Figure 4-9 showed the initial charge-discharge curves of the TiH_2 electrode between 1.0 V and 0.05 V using $LiBH_4$ solid electrolyte under the current density of 400 mA g^{-1} at 120 °C. The Li insertion curve showed two slopes; slope region 1 (0.4 V – 0.15 V vs. Li^+/Li) and slope region 2 (0.15 V vs. Li^+/Li). From the previous report [4-7], it was considered that the slope 1 indicated that fcc-TiH_2 (fcc: face-centered cubic) reacted with lithium to form xLiH and transformed partially into a distorted orthorhombic phase fco-TiH_{2-x} (fco: face-centered orthorhombic), and slope 2 indicated that both of fcc-TiH_2 and fco-TiH_{2-x} react with lithium to form Ti and LiH ($TiH_2 + 2Li^+ + 2e^- \rightarrow Ti + 2LiH$). Unlike the case of MgH_2, no plateau was observed below 0.15 V, indicated Ti didn't electrochemically react with Li to form Li-Ti alloy. During the initial Li insertion, the capacity of 1225 mAh g^{-1} was obtained, while the theoretical capacity was 1074 mAh g^{-1}. This overcapacity could be due to the existence of acetylene black in the electrode, which contributes on the Li storage capacity as an anode.

On the Li extraction curve, the plateau corresponding to de-lithiation process of TiH_2 conversion reaction was observed at higher voltages than 0.15 V, indicating the higher polarization of electrode compared with the case of MgH_2 system [4-8]. Furthermore, a short plateau at 0.75 V was observed and the whole Li extraction curve showed 1052 mAh g^{-1} corresponding to 86% coulombic efficiency.

In order to identify the electrochemical reaction, ex-situ XRD measurements were performed at the different states-of-charges as shown in Figure 4-10, where the roman

numbers (i) ~ (vi) correspond to states-of-charge shown in Fig. 4-9. It is noteworthy that all the profiles shown in Fig. 4-10 contain peaks corresponding to $LiBH_4$, which should always be included in the electrodes. At the initial state (i), the broad peaks corresponding to TiH_2 were observed since the composite electrode was prepared by ball milling treatment. After Li insertion (ii), the broad peaks slightly shifted to higher angle, indicating that the TiH_2 structure should be slightly shrunk due to partial extraction of hydrogen. And small peaks corresponding to fco-TiH_{2-x} and Ti were observed. With further lithiation (iii), it was clearly observed that the TiH_2 transformed into Ti and LiH. For the Li extraction process, H atoms were transferred from LiH to Ti. Then, as shown in Fig. 4-10 (iv, v), peaks corresponding to TiH_2 were reappeared, then the Ti peak was strongly reduced. These facts indicate that TiH_2 electrode reveals high electrochemical performance by using the all-solid-state cell. Actually, both of MgH_2 and TiH_2 anodes for liquid electrolyte systems haven't shown such a high coulombic efficiency. The combination of hydride and borohydride for anode and electrolyte, respectively, could lead to a better performance.

Unfortunately, the reaction at 0.75 V as shown in Fig. 4-9 was not clarified yet even though we have performed the XRD measurements at various states-of-charge. As one of the possible reasons, it could be caused by the Li extraction process from acetylene black, which cannot be detected by XRD due to its amorphous feature.

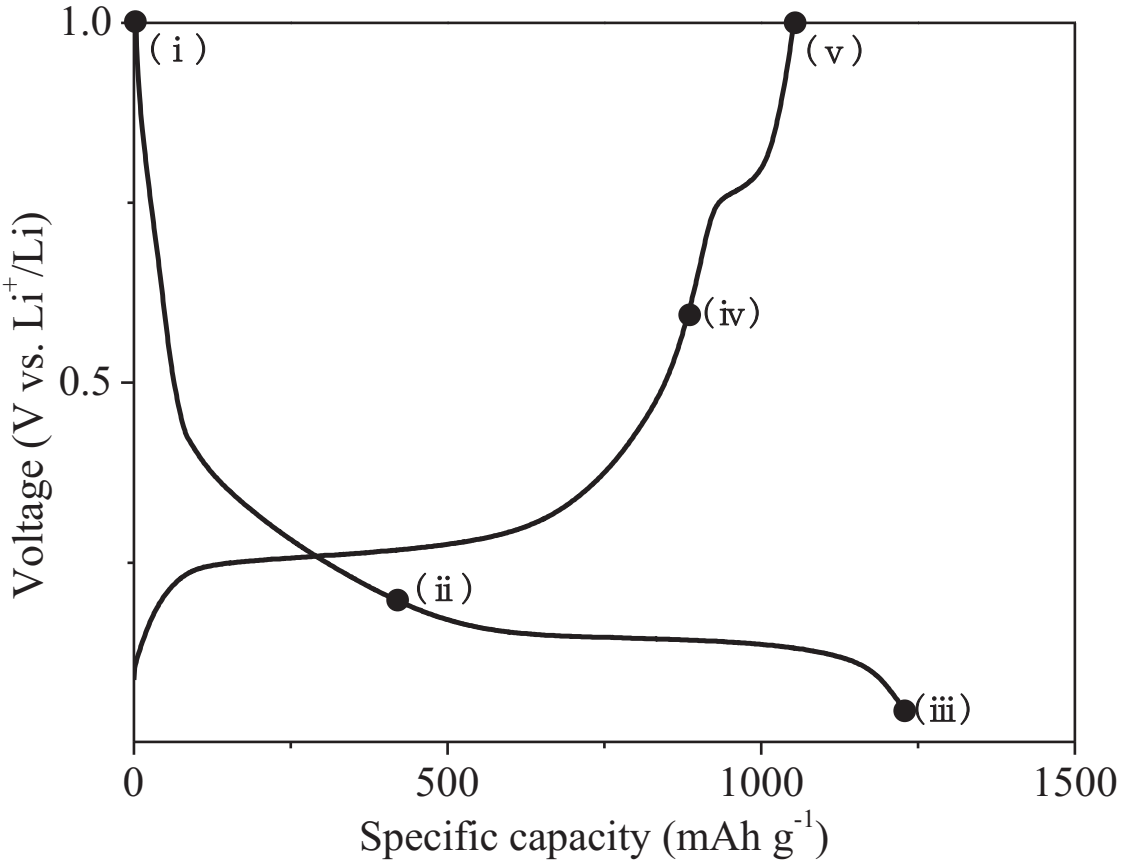

Figure 4-9 First galvanostatic charge–discharge curves for TiH_2-$LiBH_4$ electrode in the voltage range of 2.0 V – 0.05 V at a current density of 400 mAh g^{-1} at 120 °C

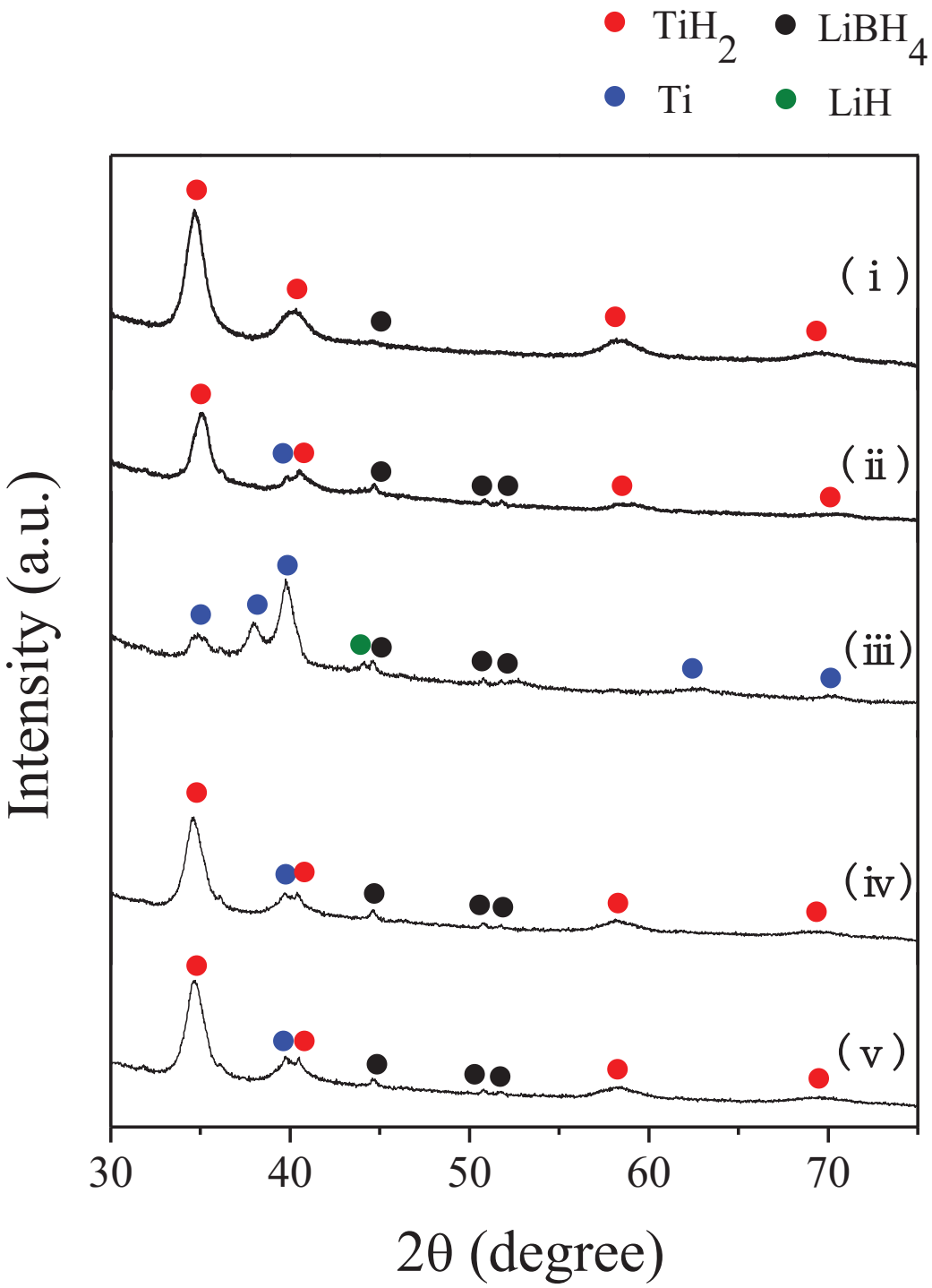

Figure 4-10 Ex-situ XRD patterns of TiH_2-$LiBH_4$ at the various states-of-charge

4.2.3 Cycle and rate properties of TiH_2 conversion reaction

Figure 4-11 showed the cyclic performance of TiH_2–$LiBH_4$ composite electrode in the voltage range of 1.0 V – 0.05 V at a current density of 400 mA g^{-1} at 120 °C. Almost the same profile as the initial cycle was observed in later cycles. The Li insertion capacities of 2^{nd}, 10^{th}, and 20^{th} cycles were 1094, 1035 and 990 mAh g^{-1}, respectively. Corresponding capacity retention after the 50^{th} charge-discharge cycles of about 80% for this TiH_2-$LiBH_4$ system is much better than that of 50% for the previous MgH_2-$LiBH_4$ [4-8] system. This result revealed for the first time that the charge-discharge process of TiH_2 electrode is recyclable, which makes it a promising candidate for lithium-ion batteries. While the reason of the 20% degradation after 50 cycles could be due to mechanical factor such as agglomeration of Ti species and/or detachment due to volume expansion, for a practical utilization, the detailed mechanism should be clarified as further research.

The rate capability of the TiH_2 composite electrode was also investigated as shown in Figure 4-12. All the discharge profiles in this figure were created by the initial discharge cycle of independent cells at different current densities of 400, 800, and 1600 mA g^{-1}. It can be seen that discharge capacities were 1225, 1165 and 1007 mAh g^{-1} at the current density of 400, 800, and 1600 mA g^{-1}, respectively, indicated a good rate capability of TiH_2 electrode in this system. For comparison, the charge-discharge for TiH_2 in a conventional organic electrolyte could be performed only at 10 mA g^{-1} [4-9]. The fast kinetics could be ascribed to rapid Li^+ and H^- diffusion in the electrode material and on

the electrode–electrolyte interface at a high working temperature of 120 °C. It was noteworthy that the average voltage gradually decreased along with the increasing discharge rate, while the theoretical equilibrium potential of this conversion reaction was 0.163 V versus Li^+/Li. It was considered that the decrease of equilibrium potential could be caused by the insufficiency of electronic conductivity at high current density, which can be improved by surface modification such as carbon coating or other technique.

Figure 4-13 showed cyclic stability curves of the TiH_2–$LiBH_4$ composite electrode at current density of 400, 800, and 1600 mA g^{-1} at 120 °C. The capacity showed rapid degradation at current density of 800 and 1600 mA g^{-1}, meaning that the material was damaged during fast charge-discharge. On the other hand, in the case of 400 mA g^{-1}, 669 mAh g^{-1} was obtained even after 100 cycles with better capacity retention curve.

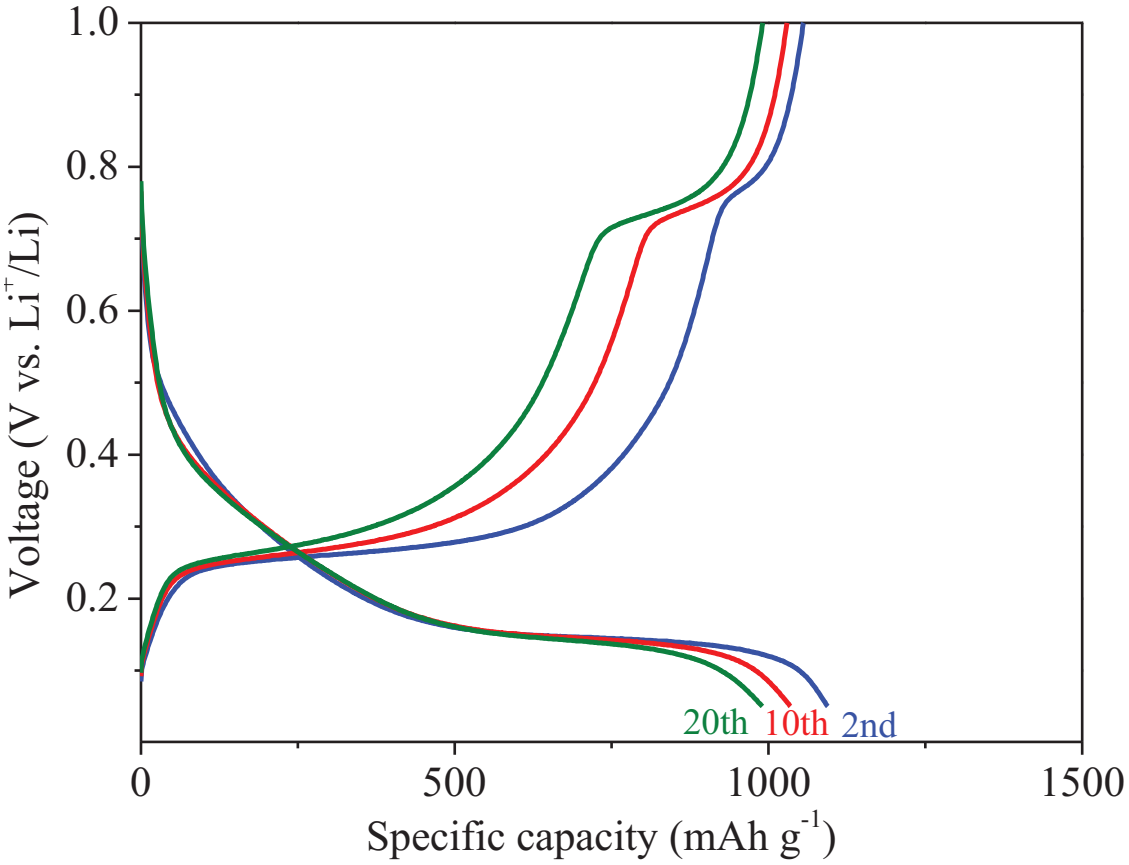

Figure 4-11 Cyclic performances of the TiH_2–$LiBH_4$ composite electrode in the voltage range of 1.0 V–0.05 V at a current density of 400 mA g^{-1} at 120 °C

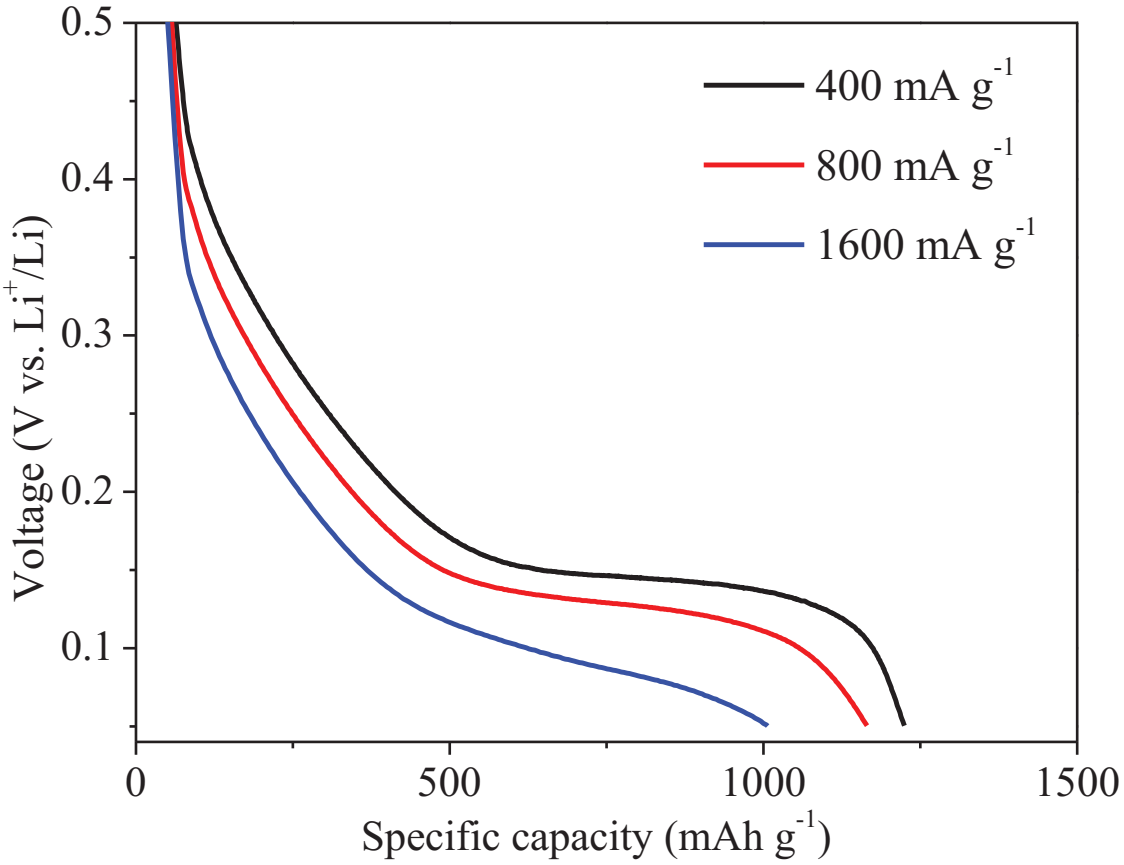

Figure 4-12 Rate capability of the TiH_2–$LiBH_4$ composite electrode at a current density of 400, 800 and 1600 mA g^{-1} at 120 °C

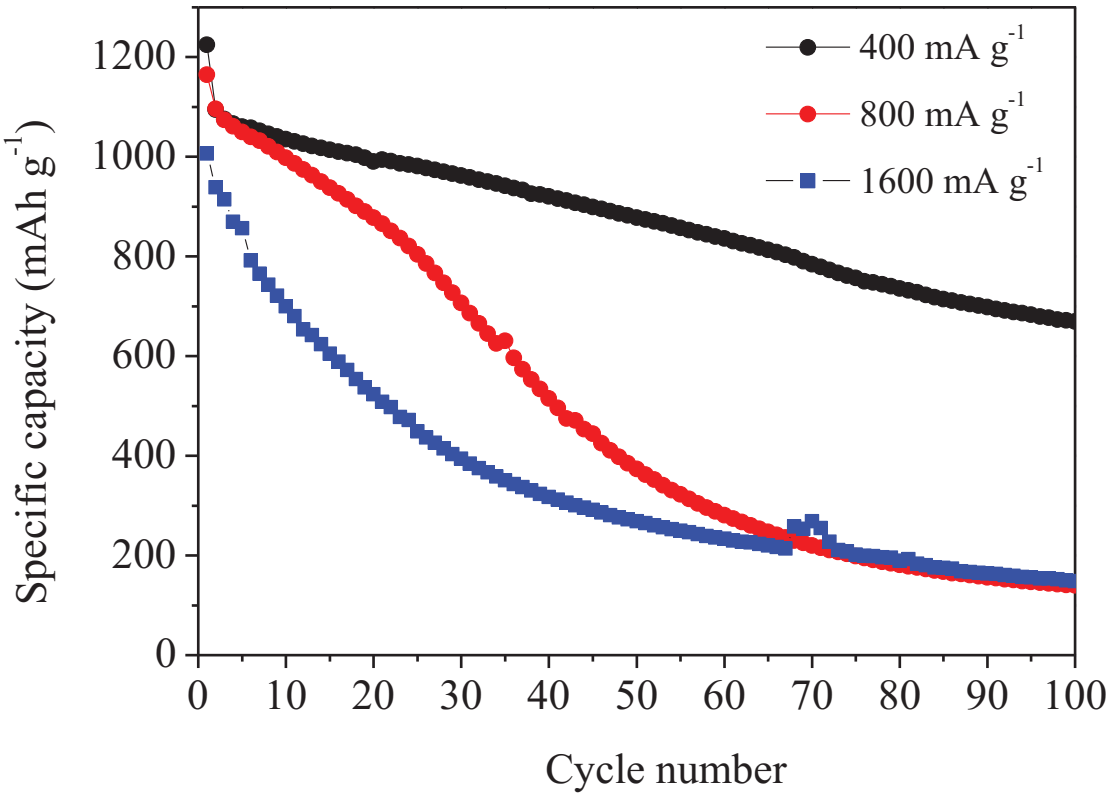

Figure 4-13 Cyclic stability curves of the TiH_2–$LiBH_4$ composite electrode in the voltage range of 1.0 V–0.05 V at current density of 400, 800 and 1600 mA g^{-1} at 120 °C

4.2.4 Summary

In this work, TiH_2 was performed as a negative electrode material for lithium ion batteries by using $LiBH_4$ solid electrolyte. The good reversibility of TiH_2 conversion reaction was observed by using XRD. Although the capacity decreased rapidly as increasing the current density, the TiH_2-$LiBH_4$ composite electrode system showed better electrochemical properties than previous report of conventional liquid electrolyte system. Taking the in-situ FT-IR results into consideration, it was considered that the hydrogen exchange effect enhanced the mobility of H^- in TiH_2 as is the case with MgH_2-$LiBH_4$ composite electrode.

[4-1] Y. Oumellal, A. Rougier, G.A. Nazri, J.M. Tarascon, L. Aymard, Nat. Mater., 7 (2008) 916-921.

[4-2] Z.Z. Fang, X.D. Kang, P. Wang, H.W. Li, S.I. Orimo, J. Alloys Compd., 491 (2010) L1-L4.

[4-3] E.G. Bardaji, Z. Zhao-Karger, N. Boucharat, A. Nale, M.J. van Setten, W. Lohstroh, E. Rohm, M. Catti, M. Fichtner, J. Phys. Chem. C, 115 (2011) 6095-6101.

[4-4] P. Verma, P. Maire, P. Novak, Electrochimica Acta, 55 (2010) 6332-6341.

[4-5] C.D. Gu, W. Yan, J.L. Zhang, J.P. Tu, Corros. Sci.

[4-6] L. Zeng, H. Miyaoka, T. Ichikawa, Y. Kojima, J. Phys. Chem. C, 114 (2010) 13132-13135.

[4-7] Y. Oumellal, W. Zaidi, J.P. Bonnet, F. Cuevas, M. Latroche, J. Zhang, J.L. Bobet, A. Rougier, L. Aymard, Int. J. Hydrogen Energy, 37 (2012) 7831-7835.

[4-8] L. Zeng, K. Kawahito, S. Ikeda, T. Ichikawa, H. Miyaoka, Y. Kojima, Chem. Commun., 51 (2015) 9773-9776.

[4-9] L. Aymard, Y. Oumellal, J.P. Bonnet, Beilstein J. Nanotechnol., 6 (2015) 1821-1839.

5 Conclusions

In this thesis, MgH_2 and TiH_2 were utilized as a negative electrode material for lithium ion batteries by using $LiBH_4$ solid electrolyte. The detailed electrochemical reaction processes and cyclability of the electrode materials have been studied and discussed.

•MgH_2

The charge-discharge processes of MgH_2-$LiBH_4$ composite electrode were studied by using ex-situ XRD measurement. The result showed that MgH_2-$LiBH_4$ composite exhibited reversible electrochemical reaction of MgH_2 conversion reaction (0.5 V vs. Li^+/Li), Li-Mg alloying reaction (0.1 V vs. Li^+/Li) as similar to previous report of liquid electrolyte system. Meanwhile, unexpected electrochemical reaction of a generation of $Mg(BH_4)_2$ (0.8 – 1.2 V vs. Li^+/Li) was observed in this solid electrolyte system. To investigate the cyclability of these electrochemical reactions, charge-discharge measurements were performed with controlling working voltage windows between 2.0 – 0.05 V, 1.0 – 0.05 V and 1.0 – 0.3 V. The results showed that large degradation on the capacity was found caused by the $Mg(BH_4)_2$ conversion and the Li-Mg alloying process, except for only MgH_2 conversion reaction. By optimizing the cut-off voltage, MgH_2 can work as high performance electrode in this system. This system showed quite higher reversible capacity and smaller charge-discharge polarization than in the case of conventional liquid electrolyte system.

•TiH_2

It was clarified that TiH_2-$LiBH_4$ composite had the hydrogen exchange effect similar to MgH_2-$LiBH_4$ composite. Focusing on the phenomenon, the $LiBH_4$ solid electrolyte was applied to TiH_2 electrode. Similarly to the previous report by using a conventional liquid electrolyte, two kinds of slope regions were observed in the Li insertion curve, which correspond to fco-TiH_{2-x} and Ti generations, respectively. In addition, the good reversibility of TiH_2 conversion reaction was observed by using XRD measurement. Although the capacity decreased rapidly as increasing in the current density, the TiH_2-$LiBH_4$ composite electrode system showed better electrochemical properties than previous report of conventional liquid electrolyte system. This result revealed for the first time that the charge-discharge process of TiH_2 electrode is recyclable, which makes it a promising candidate for lithium-ion batteries.

$LiBH_4$ solid electrolyte leads to excellent electrochemical properties for the both of MgH_2 and TiH_2 electrode as lithium ion batteries. It is considered that $LiBH_4$ acts as a multifunctional ion conductor and promotes not only Li^+ but also H^- conductivity, resulting in a much higher reversibility for the hydride conversion reaction. The results of this work open a new way to search for suitable negative electrode materials for lithium-ion batteries. Numerous metal hydride-based materials are expected to be investigated as negative electrode materials in this system.

.

公表論文

(1) Electrochemical Performance of Titanium Hydride for Bulk-Type All-Solid-State Lithium-Ion Batteries
Koji Kawahito, Liang Zeng, Takayuki Ichikawa, Hiroki Miyaoka and Yoshitsugu Kojima
Materials Transactions, 57, 755-757 (2016).

参考論文

(1) Metal hydride-based materials towards high performance negative electrodes for all-solid-state lithium-ion batteries
Liang Zeng, Koji Kawahito, Suguru Ikeda, Takayuki Ichikawa, Hiroki Miyaoka and Yoshitsugu Kojima
Chemical Communications, 51, 9773-9776 (2015).